Investigation of Gluon Saturation using Di-hadron Correlation and assessing Efficiency and Resolution of ePIC detector in EIC

M.SC. Thesis

Priyanshu Khemka



Investigation of Gluon Saturation using Di-hadron Correlation and assessing Efficiency and Resolution of ePIC detector in EIC

A Thesis

Submitted in partial fulfilment of the requirements for the award of the degree

of Master of Science

By

Priyanshu Khemka 2303151026



DEPARTMENT OF PHYSICS INDIAN INSTITUTE OF TECHNOLOGY INDORE MAY, 2025



INDIAN INSTITUTE OF TECHNOLOGY INDORE

CANDIDATE'S DECLARATION

I hereby certify that the work which is being presented in the thesis entitled Investigation of Gluon Saturation using Di-hadron Correlation and assessing Efficiency and Resolution of ePIC detector in EIC in the partial fulfillment of the requirements for the award of the degree of MASTER OF SCIENCE and submitted in the DEPART-MENT OF PHYSICS, Indian Institute of Technology Indore, is an authentic record of my work carried out during the period from July 2023 to May 2025 under the supervision of Dr. Ankhi Roy, Professor, Indian Institute of Technology Indore.

The matter presented in this thesis has not been submitted by me for the award of any other degree of this or any other institute.

Priyanshu Khemka 13/05/25 (Priyanshu Khemka)

This is to certify that the above statement made by the candidate is correct to the best of my knowledge.

Ankhi Ray 13/05/25 (Prof. Ankhi Roy)

Priyanshu Khemka has successfully given his M.Sc. Oral Examination held on 13th May 2025.

(DPGC Physics)

Dedicated to Maa

ACKNOWLEDGEMENT

First and foremost, I express my sincere gratitude to my project supervisor, Prof. Ankhi Roy, for her invaluable guidance and unwavering support throughout my research endeavor. I am deeply grateful to all the PhD seniors in my lab for their invaluable mentorship and assistance at every juncture. I'm also thankful to my friends for their constant support, all the beautiful memories we have created together. Lastly, I want to thank my parents for always supporting me and believing in me, which kept me focused and motivated.

Abstract

This thesis investigates the phenomenon of gluon saturation in quantum chromodynamics (QCD) by analyzing di-hadron correlations in high-energy nuclear collisions and evaluates the tracking performance of the ePIC detector for the upcoming Electron-Ion Collider (EIC). Gluon saturation, expected at high parton densities, leads to nonlinear effects that alter particle production and correlation patterns. Using data from the STAR experiment at RHIC, the study examines azimuthal correlations between pairs of hadrons in proton-proton and deuteron-gold collisions. The results reveal a significant suppression and broadening of the back-to-back (away-side) peak in central deuteron-gold collisions, providing evidence for gluon saturation effects that cannot be explained by conventional models.

The thesis also assesses the efficiency and momentum resolution of the ePIC detector through simulation studies focused on charged pion reconstruction. Both idealized (truth-seeded) and realistic (real-seeded) tracking methods are evaluated.

Overall, this work demonstrates that di-hadron correlations are a sensitive probe of gluon saturation and establishes the readiness of the ePIC detector for exploring QCD dynamics in high-density regimes.

Table of Contents

Ta	able	of Con	tents	X
Li	st of	Figur	es	xi
1	Inti	\mathbf{roduct}	ion	1
	1.1	Motiv	ation	3
	1.2	Struct	cure of the Thesis	5
2	${ m Lit}\epsilon$	erature	e Review	7
	2.1	Di-hao	dron Correlation	8
	2.2	Two-p	particle correlations in STAR	9
		2.2.1	Scientific Motivation and Background	9
		2.2.2	Experimental Setup	9
		2.2.3	Key Results	10
3	Kin	ematic	c variables and simulation methodology	12
	3.1	Kinen	natics	12
		3.1.1	Kinematic Variables in $e-p$ scattering	12
		3.1.2	Rapidity and pseudo-rapidity variables	15
		3.1.3	Transverse momentum	16
	3.2	Monte	e Carlo event generators	17
4	Sat	uration	n Framework	20
	4.1	IP-Gla	asma	20
		4.1.1	IP-Sat Model	20
		4.1.2	Model Description	22

5	Result and Analysis				
	5.1	Transverse momentum distribution	26		
	5.2	Two-particle azimuthal correlation	27		
6	The	EIC Experiment	29		
	6.1	Reference EIC detector	31		
	6.2	Track reconstruction method	35		
	6.3	Efficiency of charged pions	36		
	6.4	Momentum resolution of charged pions	38		
		6.4.1 Momentum resolution for truth seeded particles	38		
		6.4.2 Momentum resolution for real seeded particles	42		
7	Sun	nmary	46		
Aj	open	\mathbf{dix}	48		
\mathbf{A}	JET	SCAPE setting for saturation effects	49		
В	Azi	muthal angle correlation	52		
Re	efere	nces	53		

List of Figures

1.1	Proton parton distribution function plotted as a function of	
	Bjorken- x [1]	4
1.2	At small values of x (as depicted on the right), the proton's wave-function contains a significantly higher number of glu-	
	ons compared to its wave-function at a larger $x = x_0$ (shown	
	on the left)[1]. \dots	5
2.1	The small- x non-linear dynamics governing the evolution of	
	hadronic or nuclear wave functions. Straight solid lines for	
	simplicity denote all partons (quarks and gluons)	7
2.2	Feynman diagram showing gluonic interaction of jet-2 with	
	the nucleus, hence losing its momentum[3]	8
2.3	A comparison of di-hadron correlations between two for-	
	ward π^0 mesons is shown for p+p collisions (left), periph-	
	eral d+Au collisions (center), and central d+Au collisions	
	(right)[4]	10
3.1	Inelastic electron-proton scattering	13
3.2	Schematic representation of the values of pseudo-rapidity	
	(η) around the detector[18]	16
3.3	Flowchart for the JETSCAPE framework[11]	17
4.1	Feynman diagram of $q\bar{q}$ pair interacting with proton[13].	21
4.2	Schematic diagram showing that as energy increases, the	
	gluon density inside the nucleon increases	24

4.3	parameter for different proton sizes [15]
5.1	Normalized neutal-pion transverse momentum distribution from JETSCAPE
5.2	Azimuthal angle $(\Delta \phi)$ correlation between final state neutral- pions
5.3	Azimuthal angle $(\Delta \phi)$ correlation between final state neutral- pions for different multiplicity ranges
6.1	Schemaic layout of hadrons and the scattered lepton for different $x-Q^2$ distributed over the detector rapidity coverage [17]
6.2	3D model of EIC detector design[18]
6.3	A 2D schematic of an EIC detector layout[18]
6.4	A GEANT4 visualization depicts the far-forward hadron
	beam magnets in green, along with a simplified illustration
	of the beam pipe and the four detector subsystems that are
	currently part of the reference detector configuration[18]
6.5	3D schematic of an ePIC detector design[17]
6.6	Variation of efficiency with transverse momentum (p_T) of charged pions for truth-seeded track
6.7	Variation of efficiency with transverse momentum (p_T) of charged pions for truth-seeded track
6.8	Variation of efficiency with pseudo-rapidity (η) of charged pions for truth-seeded track
6.9	Momentum resolution of charged pions in $ \eta < 1$ range
6.10	Resolution across various p_T ranges, fitted with double Gaus-
	sian function
6.11	Resolution across various p_T ranges, fitted with double Gaus-
	sian function
6.12	Sigma (σ) vs p_T for charged pion at $ \eta < 1 \dots \dots$
6.13	Sigma (σ) vs p_T for charged pion at different η ranges

6.14	Momentum resolution of charged pions in $1 < \eta < 3$ range	
	for real-seeded branch	42
6.15	Resolution across various p_T ranges, fitted with double Gaus-	
	sian function	43
6.16	Resolution across various p_T ranges, fitted with double Gaus-	
	sian function	44
6.17	σ vs p_T for charged pions at $1 < \eta < 3$	44
6.18	Sigma (σ) vs p_T for charged pion at different η range	45
6.19	Comparison between truth seeded sigma (σ) vs p_T and real	
	seeded sigma (σ) vs p_T for charged pion at different η ranges.	45

Chapter 1

Introduction

Nuclear Science deals with the origins and structures of atoms, nuclei, and nucleons, accounting for the vast majority of the observed mass in the universe. Over decades of study, it has become evident that nucleons consist of even smaller building blocks known as quarks, bound by the strong force mediated by gluons. This fundamental theory describes the strong force as Quantum Chromo-Dynamics (QCD). The objective is to comprehend the intricate interactions among quarks and gluons and how nuclei and nucleons emerge from the properties and dynamics of these particles. The electron-proton (e - p) scattering is a cleaner and precise probe to study the internal structure of a nucleon.

QCD, the established theory describing strong interactions, has proven highly effective in explaining a vast range of hadronic and nuclear phenomena. One of the pivotal insights in QCD was recognizing that the strong coupling constant varies with energy—an effect known as the running coupling—leading to the concept of asymptotic freedom—the theoretical and experimental observation that gluons and quarks behave nearly as free particles when confined to very short distances within hadrons.

Deep inelastic scattering (DIS) experiments have played a crucial role in advancing our understanding of QCD. In these experiments, a high-energy lepton is scattered off a proton or nucleus, serving as a probe into its internal structure. The interaction occurs by exchanging a virtual photon, allowing the lepton to effectively "see" the quark distribution inside the target. Earlier DIS experiments have been instrumental in visualizing the partonic structure of the proton as well as that of various light and medium-mass nuclei.

DIS experiments involving heavy nuclei at high energies offer a powerful approach to exploring gluon dynamics. In such collisions, the presence of many nucleons within a heavy ion enhances the likelihood of encountering the wave function of the dense gluonic fields. This can lead to parton saturation at sufficiently high energies—a state where gluon densities become so large that non-linear QCD effects suppress their growth. This phenomenon is called the color glass condensate (CGC) [1].

The initiation of this saturation regime is characterized by a scale known as the saturation momentum, Q_s , which tends to be significantly higher in heavy nuclei. Remarkably, while the dynamics in this regime are governed by strong gluon fields and non-linear QCD interactions, the large value of Q_s permits the use of perturbative techniques. This is made possible by QCD's property of asymptotic freedom, which ensures that the coupling becomes weak at high momentum scales, enabling controlled theoretical predictions.

We outline the key physics goals of small-x experiments and the measurements required to address fundamental questions in this regime. Investigating the internal structure of nuclei at low Bjorken-x requires precise measurements of the nuclear structure functions F_2 and F_L across varying values of both x and the photon virtuality Q^2 . These measurements enable the extraction of gluon and quark distribution functions within nuclei and can provide direct evidence for the emergence of non-linear QCD phenomena.

A crucial objective is to determine the saturation scale Q_s , which characterizes the CGC state of the nucleus. This can be achieved through the analysis of two-particle correlations. Furthermore, gluons' spatial and momentum distributions can be mapped by studying the cross-sections of exclusive vector meson production. Diffractive (quasi-elastic) processes,

in particular, offer high sensitivity to the emergence of non-linear QCD effects, making them a valuable probe of gluon saturation.

1.1 Motivation

The proton, at its core, consists of three valence quarks—two up quarks and one down quark—held together by the strong force through the exchange of gluons. This basic model, however, fails to capture the full complexity of proton structure revealed by high-energy experiments. Observations from the hadron-electron ring accelerator (HERA) collider at Deutsches Elektronen-Synchrotron (DESY) in Germany, as well as results from the Large Hadron Collider (LHC) and the Relativistic Heavy Ion Collider (RHIC), show that the proton is far more dynamic. It contains a fluctuating sea of gluons and transient quark—antiquark pairs that constantly emerge and vanish due to quantum effects.

These quantum fluctuations become more apparent in high-energy scattering experiments. As a proton is accelerated to near light speeds, Lorentz time dilation causes the lifetimes of these internal fluctuations, especially gluon emissions, to appear longer to an external observer. The faster the proton moves, the more time an observer has to "see" the internal gluon activity. This makes it possible to effectively freeze and examine these fleeting processes by colliding the fast-moving proton with another high-energy particle, providing insight into its intricate substructure.

In DIS experiments, a high-energy lepton is used to probe the internal structure of the proton by exchanging a virtual photon. The squared momentum transferred by this photon, denoted as Q^2 , sets the resolution of the probe in the plane perpendicular to the beam direction. According to the uncertainty principle, the transverse size of the region being examined is roughly $\Delta r_T \sim 1/Q$. Another key parameter in DIS is the Bjorken-x, which represents the fraction of the proton's momentum carried by the quark that interacts with the photon. At high energies, this variable becomes small, as $x \approx Q^2/W^2$, where W^2 is the squared center-of-mass en-

ergy of the proton-photon system. Thus, small values of x correspond to scattering processes at very high energies.

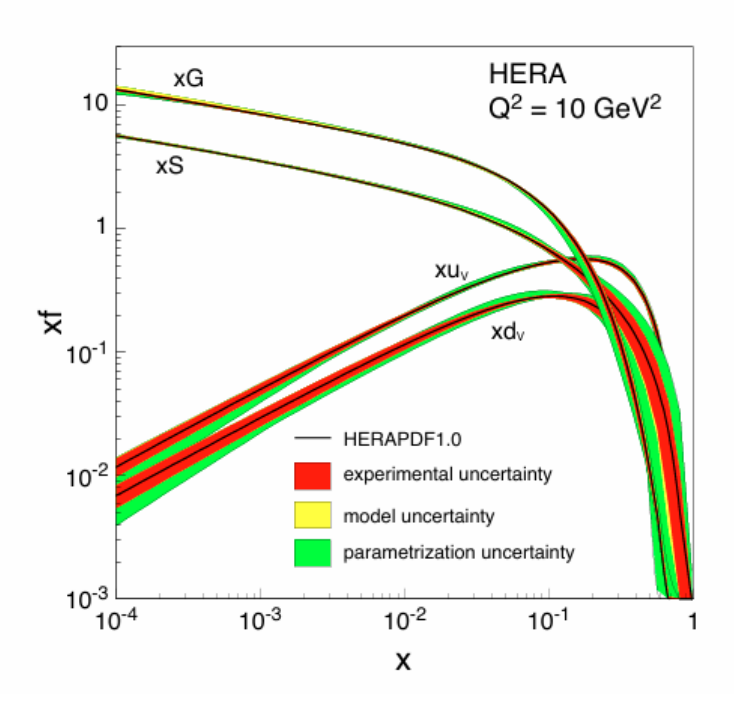


Figure 1.1: Proton parton distribution function plotted as a function of Bjorken-x [1].

The proton's wave-function is influenced by both the Bjorken-x and the momentum transfer Q^2 . This dependence is illustrated in Fig. 1.1, based on DIS data collected at HERA. The figure displays how the parton distribution functions (PDFs)—which describe the likelihood of finding a quark or gluon carrying a fraction x of the proton's momentum—vary with x. At leading order, PDFs can be interpreted as number densities of partons inside the proton. In the plot, the distributions for valence quarks, represented by xu_v and xd_v , are seen to decrease as x becomes smaller. In contrast, the distributions for sea quarks and gluons—shown as xS and xG, respectively—rise steeply at low x. (Note that the vertical axis uses a logarithmic scale.) Notably, the gluon distribution surpasses that of both valence and sea quarks for x < 0.1. Since low x corresponds to highenergy regimes, this indicates that at very high energies, the dominant contribution to the proton's wave-function comes from gluons.

At small x, the proton is filled with a dense population of gluons, es-

pecially in the transverse plane. Fig. 1.2 illustrates this by comparing the parton content of the proton at large and small x. The right panel, corresponding to the lower x, shows a significant increase in gluon density compared to the left panel, which represents higher x. This highly populated gluonic state of a fast-moving proton or nucleus is known as the CGC.

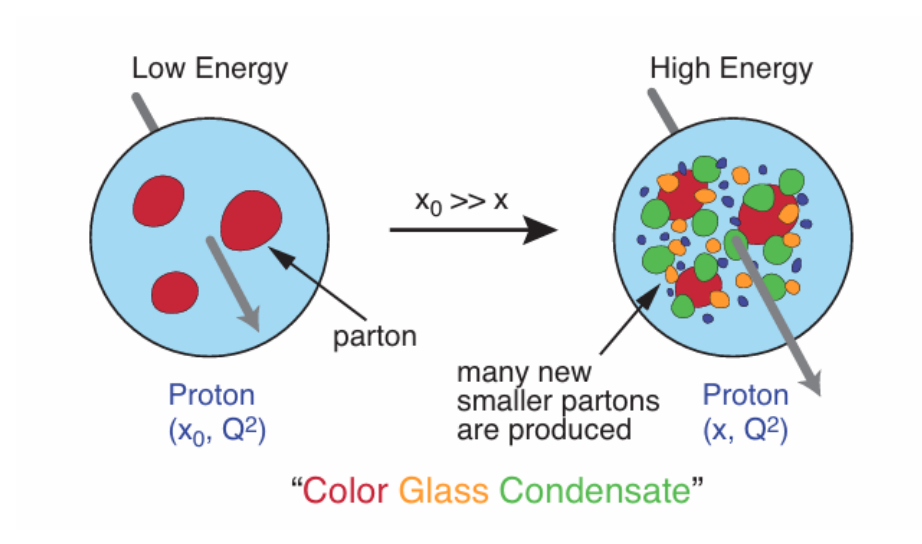


Figure 1.2: At small values of x (as depicted on the right), the proton's wave-function contains a significantly higher number of gluons compared to its wave-function at a larger $x = x_0$ (shown on the left)[1].

1.2 Structure of the Thesis

Here we will outline a brief overview of the thesis. This thesis mainly has two parts. In the first part, from chapter 2, we have phenomenological studies of gluon saturation, for which we have chosen the p-Pb system which is an easier probe to study saturation because of high energy collision. In the second part, chapter 6 is dedicated to studying the resolution and efficiency of the ePIC detector for EIC¹

• Chapter 2 is a brief overview of the literature survey to establish the problem statement of gluon saturation in the p-Pb system.

¹Electron-ion collider

- Chapter 3 focuses on the basic kinematics of the p-Pb collisions, and the event generator used to simulate the collision events.
- Chapter 4 focuses on the saturation model used to implement the CGC effects in the collision events.
- Chapter 5 focuses on the results and analysis of gluon saturation using di-hadron correlation, two-particle azimuthal correlation at center of mass energy 5.02 TeV.
- Chapter 6 discusses briefly the EIC experiment and studies the resolution and efficiency of the ePIC detector for EIC.
- Chapter 7 is the summary and outlook section of the thesis.
- **Appendix** contains the supplementary information for the reader's reference.

Chapter 2

Literature Review

Gluon saturation is a fundamental phenomenon in QCD that emerges at high energies, where the density of gluons inside protons and nuclei becomes so large that nonlinear effects, like gluon recombination, become significant. This leads to a saturated state where further increases in gluon density are suppressed, marking a transition from a dilute to a dense partonic regime. Understanding gluon saturation is crucial for decoding the behavior of hadronic matter, especially in heavy-ion collisions and in the early universe.

At small values of Bjorken x (representing low momentum fractions), gluon densities inside nucleons rise rapidly with energy. Gluon recombination processes eventually tempered this growth, which becomes significant at high densities, leading to saturation. The critical parameter here is the saturation scale, which increases with the size of the nucleus and energy, making heavy nuclei ideal for studying these effects.

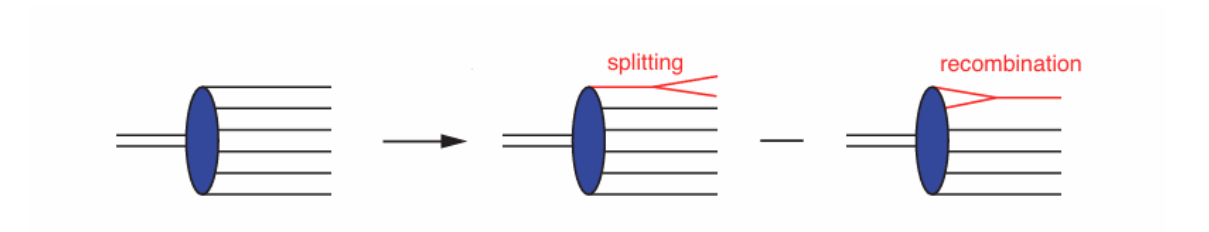


Figure 2.1: The small-x non-linear dynamics governing the evolution of hadronic or nuclear wave functions. Straight solid lines for simplicity denote all partons (quarks and gluons).

The CGC framework describes this regime, predicting that gluons at the

saturation scale behave more like classical fields than individual quantum particles. The onset of saturation is expected to alter particle production and correlation patterns in high-energy collisions.

2.1 Di-hadron Correlation

Di-hadron correlations are critical for probing gluon saturation in QCD because they reveal nonlinear dynamics in dense gluon environments that single-particle measurements cannot capture. In high-energy collisions, gluon saturation occurs when gluon densities become so high that recombination (nonlinear effects) balances splitting. Di-hadron correlations measure the angular relationship $(\Delta \phi)$ between two emitted hadrons, which is directly influenced by these gluon interactions [3].

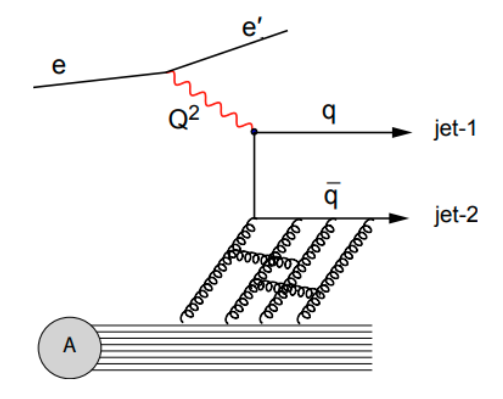


Figure 2.2: Feynman diagram showing gluonic interaction of jet-2 with the nucleus, hence losing its momentum[3].

In the saturation regime, a large transverse momentum imbalance for the hadron pair is expected (Fig. 2.2), which leads to back-to-back jet/hadron pairs to decorrelate, which leads to a suppression in the away-side peak. In proton-nucleus (p+A) collisions, the back-to-back ($\Delta \phi \approx \pi$) correlation peak observed in proton-proton (p+p) collisions is suppressed. This suppression arises from multiple scatterings and gluon recombination in the saturated nuclear medium, a hallmark of saturation physics. Saturation effects increase the transverse momentum spread of hadrons, weakening azimuthal correlations.

2.2 Two-particle correlations in STAR

This paper presents results from the STAR experiment at RHIC, focusing on azimuthal correlations of two-particle at forward rapidity in both deuteron-gold (d+Au) and proton-proton (p+p) collisions at a center-of-mass energy of $\sqrt{s_{NN}} = 200$ GeV. The study leverages the enhanced acceptance provided by the Forward Meson Spectrometer (FMS), enabling sensitivity to gluon densities at very low Bjorken-x ($x \sim 10^{-3}$). The main goal is to probe gluon saturation effects in nuclei, as predicted by the CGC framework[4][5].

2.2.1 Scientific Motivation and Background

Two-particle correlations are a sensitive probe for distinguishing between dilute and saturated partonic systems. In leading-order perturbative QCD (pQCD), high-energy hadron collisions typically produce back-to-back jets, leading to a characteristic peak at $\Delta \phi \sim \pi$ in azimuthal correlations[8].

Gluon saturation is expected at high parton densities, where the standard $2 \to 2$ parton scattering picture breaks down. Instead, a probe parton can interact with multiple gluons (see Fig. 2.2), leading to a broadening or disappearance of the back-to-back correlation (the "away-side" peak). The CGC model describes this high-density regime, predicting that at sufficiently low x, gluon recombination leads to collective recoil and modified correlation patterns.

2.2.2 Experimental Setup

The STAR experiment's forward rapidity measurements rely on upgrades to its detector systems, enabling precise tracking and calorimetry in the pseudorapidity range $2.5 < \eta < 4.0$. Key components include:

1. Trigger and Acceptance

• Events are triggered by a forward π^0 (2.5 < η < 4) detected via its two-photon decay in the Forward Meson Spectrometer (FMS).

• Associated particles are measured in the Barrel/Endcap EM Calorimeters ($|\eta| < 2.0$) or FMS, enabling azimuthal correlation studies across rapidity gaps.

This configuration allows the selection of events where a parton with high-x (from the projectile) interacts with a gluon with low-x (from the target nucleus), probing the saturation regime at $x \sim 10^{-3}$.

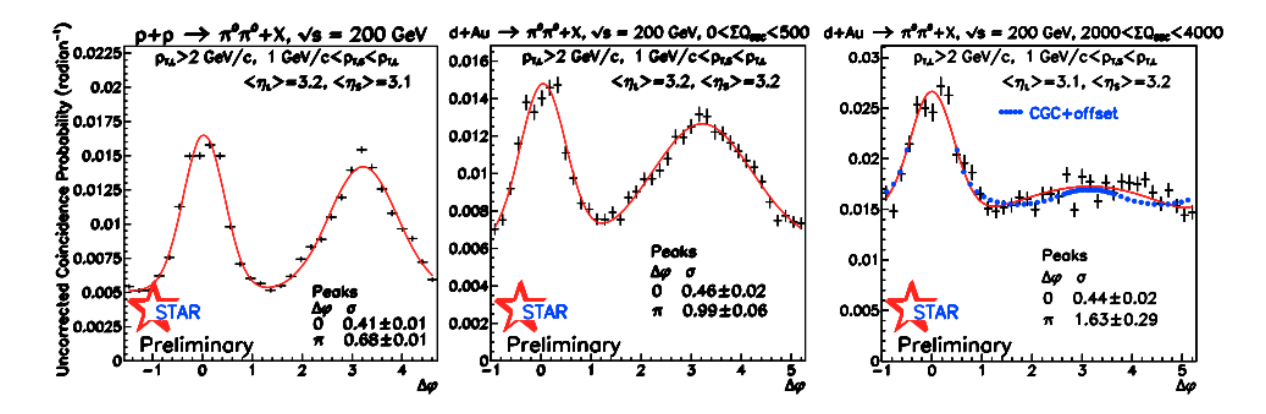


Figure 2.3: A comparison of di-hadron correlations between two forward π^0 mesons is shown for p+p collisions (left), peripheral d+Au collisions (center), and central d+Au collisions (right)[4].

2.2.3 Key Results

- 1. Azimuthal Correlation Measurements: The study systematically measures the azimuthal angle difference ($\Delta \phi$) between a forward π^0 and an associated particle. The focus is on the comparison between p+p and d+Au collisions, and on the centrality dependence in d+Au[10].
- 2. Broadening and Suppression of the Away-side Peak:
 - In p+p and peripheral d+Au collisions, the back-to-back (away-side) peak at $\Delta \phi \sim \pi$ is prominent, though slightly broadened in peripheral d+Au[5][6][7].
 - In central d+Au collisions, the away-side peak is strongly suppressed and significantly broadened, while the near-side peak ($\Delta \phi \sim 0$) remains unchanged[9].

3. Comparison with CGC Predictions: In central d+Au collision, a suppression is observed, which is qualitatively consistent with CGC calculations, which predict such effects due to gluon saturation in the nucleus.

4. Systematic Studies:

- Simulations using PYTHIA (with various parton distribution functions) and HIJING were performed to assess the impact of increased multiplicity and combinatorial background in d+Au events.
- The suppression of the away-side peak is not reproduced by these conventional models, nor is it attributable to increased event multiplicity or background effects, strengthening the case for saturation physics.

The STAR data, especially in p+p, are sensitive to the gluon distribution at low x. The suppression and broadening of the away-side peak in central d+Au collisions, absent in p+p and not explained by conventional models, are consistent with the onset of gluon saturation as described by the CGC framework. Systematic checks confirm that the observed effects are not artifacts of increased multiplicity or combinatorial background. These results provide strong evidence that RHIC, with the STAR detector and the FMS, can access the saturation regime in nuclear gluon distributions, offering valuable insights into the non-linear dynamics of QCD at high parton densities.

Chapter 3

Kinematic variables and simulation methodology

In this chapter, the focus lies on explaining the kinematic variables involved in heavy-ion collisions. We explore the kinematics variables involved in e-p collisions, as it is easy to understand the kinematics of the DIS experiment. Furthermore, the event generator used to simulate the p-Pb collision events will be discussed.

3.1 Kinematics

The DIS process of an electron with a proton can be written as

$$e(p_1) + p(p_2) \to e'(p_3) + X(p_4)$$

where e, p refer to the incident electron and proton, e' is the scattered electron, and X is the system of particles that are produced in this interaction, p_1 , p_2 , p_3 , and p_4 are their corresponding four momenta. The kinematic variables x, Q^2 , y, and W^2 described below have intuitive physical interpretations.

3.1.1 Kinematic Variables in e-p scattering

Fig. 3.1 shows a diagram of an electron-proton collision. In this diagram, the initial four momenta of the electron and proton are labeled p_1 and p_2 , respectively, and the four momenta of the final particles are labeled p_3 and

 p_4 . Here, p_4 is the collective four-momentum of all the particles broken from the proton.

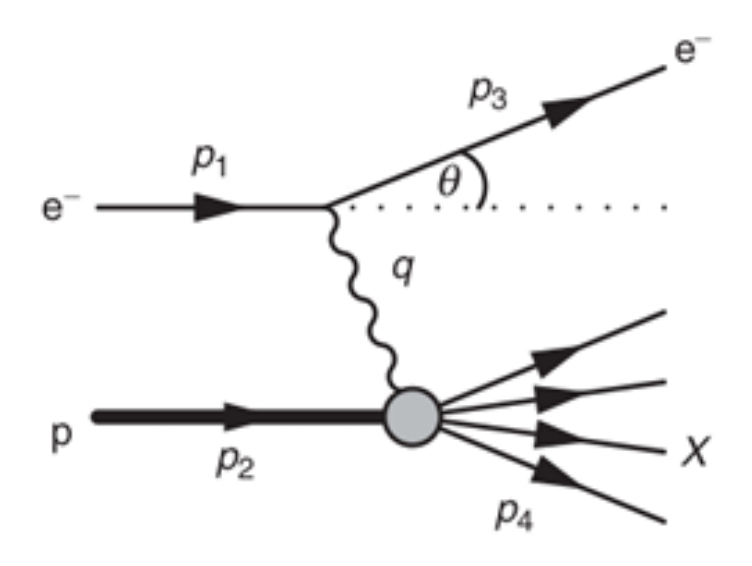


Figure 3.1: Inelastic electron-proton scattering

The momentum transfer that occurs between the electron and the proton manifests as the exchange of a virtual photon with a four-momentum of $q = p_1 - p_3$. To simplify calculations across reference frames, the Lorentz invariant quantity q^2 is used to describe the momentum transfer. Yet, q^2 is a negative quantity, so the convention is to use a positive value labeled as Q^2 , where

$$Q^2 = -q^2 \tag{3.1}$$

 Q^2 is always positive.

The Lorentz invariant dimensionless quantity Bjorken x,

$$x \equiv \frac{Q^2}{2p_2.q} \tag{3.2}$$

in the study of DIS, plays a vital role as a kinematic variable. It can be interpreted in the quark-parton model as the fraction of the proton's momentum that a parton carries. The invariant mass of the outgoing hadronic constituents is

$$W^2 \equiv p_4^2 = (p_2 + q)^2 \tag{3.3}$$

W is also the CM energy of γp system, therefore x becomes,

$$x = \frac{Q^2}{Q^2 + W^2 - m_p^2} \tag{3.4}$$

 m_p is the mass of the proton, $W^2 \equiv p_4^2 \geq m_p^2$ and $Q^2 \geq 0$, we have

$$\boxed{0 \le x \le 1} \tag{3.5}$$

The value of x is the measure of "elasticity" of the scattering process. Another dimensionless Lorentz invariant quantity is y.

$$y \equiv \frac{p_2 \cdot q}{p_2 \cdot p_1} \tag{3.6}$$

In the rest frame of the proton, $p_2 = (m_p, 0, 0, 0)$ and the momentum of the virtual photon, $q = (E_1 - E_3, p_1 - p_3)$ and therefore,

$$y = 1 - \frac{E_3}{E_1} \tag{3.7}$$

 E_1 and E_3 are the energies of the incoming and scattered electrons, respectively. It is easy to see that,

$$\boxed{0 \le y \le 1} \tag{3.8}$$

y is the fraction of energy lost by the electron in the rest frame of the proton.

In the lab frame, it is given by,

$$y = 1 - \frac{E_3}{E_1} \cos^2 \frac{\theta}{2} \tag{3.9}$$

3.1.2 Rapidity and pseudo-rapidity variables

At relativistic energy, the rapidity variable is defined as,

$$y = \frac{1}{2} \ln \left(\frac{E + p_z}{E - p_z} \right) = \frac{1}{2} \ln \left(\frac{1 + p_z/E}{1 - p_z/E} \right)$$
 (3.10)

or,

$$y = \tanh^{-1} \left(\frac{p_z}{E} \right) \tag{3.11}$$

It is a more appropriate quantity than the longitudinal velocity $(\beta_l = \frac{p_z}{E})$. The advantage of rapidity is that it is additive under a longitudinal boost, and the difference between the rapidities of two particles is invariant for the boost along the z-axis.

The relationship between the rapidity y of a particle in the laboratory frame F and the rapidity y' in a boosted frame F' which moves with a velocity β in the z-direction is,

$$y' = y - \frac{1}{2} \ln \left(\frac{1+\beta}{1-\beta} \right) \tag{3.12}$$

The only problem with rapidity is that we have to measure the energy and momentum of the particle, which is not easy. This leads to the concept of pseudo-rapidity.

For a particle emitted at an angle θ to the beam axis, the rapidity is given by,

$$y = \frac{1}{2} \ln \left(\frac{E + p_z}{E - p_z} \right) = \frac{1}{2} \ln \left(\frac{\sqrt{m^2 + p^2} + p \cos \theta}{\sqrt{m^2 + p^2} - p \cos \theta} \right)$$
(3.13)

at very high energy, p >> m, mass can be neglected,

$$y = \frac{1}{2} \ln \left(\frac{p + p \cos \theta}{p - p \cos \theta} \right)$$
$$= -\ln \tan \theta / 2 \equiv \eta$$
 (3.14)

 η is called pseudo-rapidity. For this, only θ measurement is required. It is a convenient parameter for experiments when details of the particle, e.g.,

mass, momentum, etc., are not known, but only the angle of emission is known, see figure 3.2. For $\eta = 0$, we have θ with respect to beam axis is 90° and for $\theta = 0$ or 180° , η is large.

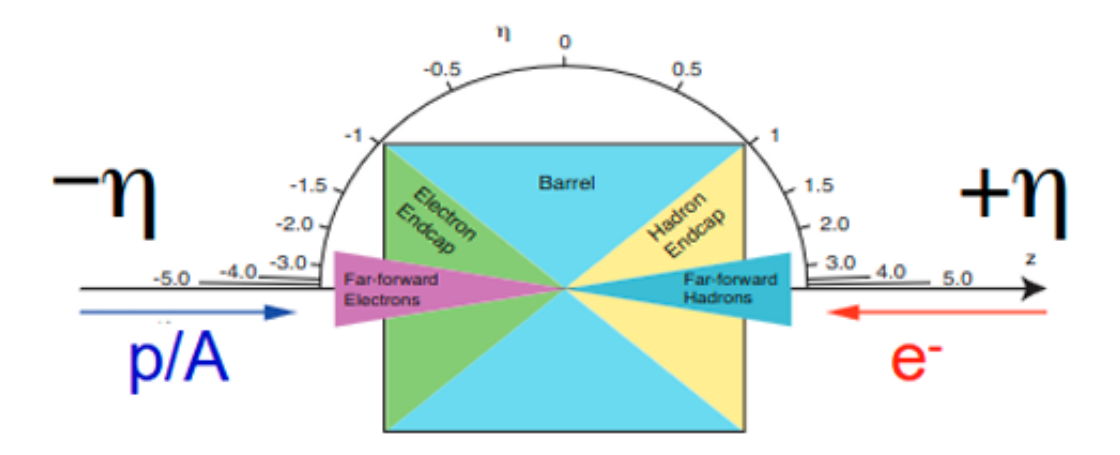


Figure 3.2: Schematic representation of the values of pseudo-rapidity (η) around the detector[18]

3.1.3 Transverse momentum

As the name suggests, transverse momentum is the transverse or perpendicular component of the total momentum of a particle with respect to the beam axis (z-axis). It is denoted by p_T , and given by

$$p_T = \sqrt{p_x^2 + p_y^2} (3.15)$$

Transverse momentum is a key factor in understanding collisions. It provides insights into the initial conditions of the collision and the behavior of particles during and after the collision. Before a collision, there's no sideways momentum. But after the collision, any sideways movement a particle has comes from the collision itself. So, by looking at how much sideways momentum particles have, we can learn a lot about what happened during the collision. We'll explore this idea further in the upcoming sections.

3.2 Monte Carlo event generators

The Monte Carlo method is a technique that is used to solve problems using random numbers and probabilities. It's widely used in numerical analysis and simulating natural processes. In particle physics, Monte Carlo generators create theoretical simulations of real events, helping scientists understand particle interactions in experiments. Different Monte Carlo generators often simulate different physics models, using matrix elements, PDFs, evolution equations, parton showers, or hadronization models. The few major general-purpose event generators are given below

- PYTHIA
- HERWIG
- SHERPA
- JETSCAPE

In the current study, JETSCAPE is used. A detailed description can be found in.

In JETSCAPE, the collision processes (in our case, p-Pb collisions) are modeled as a series of sub-processes[11].

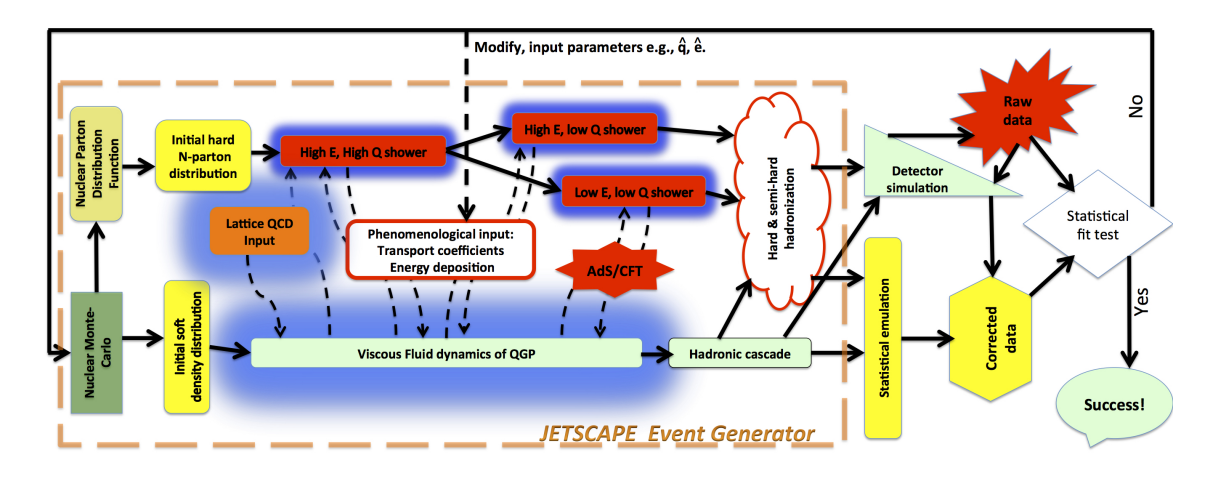


Figure 3.3: Flowchart for the JETSCAPE framework[11]

• Initial State Configuration

- 3D MC-Glauber Model: Represents nucleons as three hotspots with Gaussian spatial distributions (width ~0.5 fm). Proton and Pb nuclei positions are sampled event-by-event. Overlaps of colliding hotspots generate initial energy density via a wounded hotspot model. Parameters (hotspot cross-sections, fluctuation scales) are XML-configurable. Preferred for studying centrality-dependent observables where nucleon position fluctuations dominate (e.g., high-multiplicity p-Pb).
- IP-Glasma Model: Models nuclei as color charge distributions using the IPSat parametrization. Gluon saturation scales (Q_s) are energy-dependent, with JIMWLK evolution for small-x dynamics. Solves Yang-Mills equations post-collision to generate initial gluon fields (flux tubes) and $T^{\mu\nu}$. Critical for low- p_T observables sensitive to gluon saturation (e.g., ridge correlations in p-Pb).

• Pre-Equilibrium Dynamics

- MC-Glauber Path: Skips pre-equilibrium phase; energy density is directly fed to hydrodynamics.
- IP-Glasma Path: Includes Yang-Mills evolution (up to $\tau \sim 0.6$ fm/c) to model Glasma field dynamics before hydrodynamics.

• Hydrodynamic Evolution

- MUSIC Hydrodynamics: Evolves the medium using (2+1)D viscous hydrodynamics. Input initial conditions depend on the chosen model:
 - * MC-Glauber: Smooths energy density via a Gaussian kernel (width ~ 0.4 fm).
 - * IP-Glasma: Uses the energy momentum tensor $T^{\mu\nu}$ directly.

- Common Parameters:

* Shear viscosity: $\eta/s(T) = 0.08 \times (T/T_c)^2$ (peaking near $T_c \approx 160$ MeV).

* Freeze-out: $T_f = 154 \text{ MeV}.$

• Jet Energy Loss

- Initial Radiation: i-MATTER handles vacuum-like radiation from hard scatterings located at MC-Glauber hotspots or IP-Glasma flux tubes.
- Medium Interaction: MATTER simulates in-medium splitting with energy loss rates dependent on the local medium temperature (from hydrodynamics).

• Hadronization and Final State

- Cooper-Frye: iSS converts hydrodynamic output to hadrons.
- SMASH Afterburner: Simulates hadronic rescattering, improving agreement with $p_T < 2$ GeV spectra.

Chapter 4

Saturation Framework

This section deals with the theoretical background of the initial state of heavy-ion collisions and motivates the rest of the thesis. We will discuss the IP-Sat and the IP-Glasma model, the dipole-dipole interaction theory, and how it is related to the saturation energy[12].

4.1 IP-Glasma

IP-Glasma is designed to model the distribution of color charges in nuclei using the IP-Sat (Impact Parameter dipole Saturation) framework[13][14][15]. It calculates the color charge configurations and then evolves the corresponding gauge fields over time by solving the classical Yang-Mills (CYM) equations. Ultimately, IP-Glasma determines the system's stress-energy tensor, which is then diagonalized to extract the local energy density and flow velocity—quantities essential for initializing hydrodynamic simulations. While the classical Yang-Mills dynamics have already been discussed, this section focuses on the core aspects of the IP-Sat model, the stochastic sampling of nucleons, and the procedure used to compute the color charge density in the incoming nuclei before collision.

4.1.1 IP-Sat Model

The Impact Parameter Saturation (IP-Sat) dipole model [13] can be naturally extended to describe DIS processes involving nuclei. This approach

allows for the investigation of nuclear effects, including comparisons with experimental data related to nuclear shadowing. Additionally, it enables an estimation of the saturation scale in heavy nuclear systems.

In the dipole framework, the interaction between a virtual photon (γ^*) and a proton unfolds in three distinct stages. Initially, the virtual photon splits into a quark-antiquark $(q\bar{q})$ pair. This pair then undergoes elastic scattering off the proton. Finally, the quark-antiquark pair recombines to form the outgoing virtual photon. This sequence is illustrated schematically in Fig. 4.1. The total amplitude for the process is given by the product of the amplitudes for each step. We now examine each stage in detail.

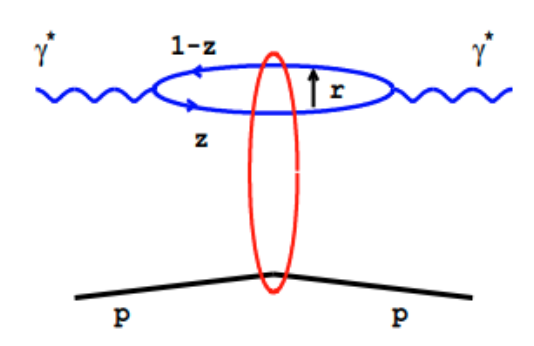


Figure 4.1: Feynman diagram of $q\bar{q}$ pair interacting with proton[13].

The amplitude describing the fluctuation of an incoming virtual photon, characterized by polarization $(\lambda = +, -, 0)$ into a quark-antiquark pair of flavor f, with helicities $h, \bar{h} = \pm \frac{1}{2}$, is represented by the light-cone wave function of the photon, denoted as $(\psi_{\gamma,f})^{h\bar{h}}_{\lambda}$. The light-cone wave function $(\psi_{\gamma,f})^{h\bar{h}}_{\lambda}$ depends on three key variables: the photon virtuality Q^2 , the longitudinal momentum fraction z carried by the quark, and the transverse separation r between the quark and antiquark. These wave functions are calculated using light-cone perturbation theory at leading order in the quark's electromagnetic coupling [10]. The amplitude for the reverse process, where the quark-antiquark pair recombines into a virtual photon, is given by the complex conjugate wave function $(\psi_{\gamma,f}^*)^{h\bar{h}}_{\lambda}$.

The elastic scattering amplitude, $A_{el}^{q\bar{q}}(x,r,\Delta)$, is well described by the

squared momentum transfer $\Delta^2 = -t$ for the elastic scattering of the $q\bar{q}$ pair. Here A_{el} is defined such that the elastic $q\bar{q}$ cross section is

$$\frac{d\sigma_{q\bar{q}}}{dt} = \frac{1}{16\pi} |A_{el}(x, r, \Delta)|^2 \tag{4.1}$$

The S-matrix element at a particular impact parameter b is defined as

$$S(b) = 1 + \frac{1}{2} \int d^2 \Delta e^{ib \cdot \Delta} A_{el}^{q\bar{q}}(x, r, \Delta)$$

$$\tag{4.2}$$

This interpretation aligns with the intuitive concept of impact parameter primarily when the dipole size is much smaller than the proton's overall size. The total cross section for the $q\bar{q}$ pair is obtained by taking the imaginary part of the elastic scattering amplitude iA_{el} , or, equivalently, it can be expressed in terms of the S-matrix element[16].

$$\sigma_{q\bar{q}}(x,r) = ImiA_{el}^{q\bar{q}}(x,r,0) = \int d^2b2(1 - Re\ S(b))$$
 (4.3)

Hence, the quark-antiquark differential cross section is given by

$$\frac{d\sigma_{q\bar{q}}}{d^2b} = 2(1 - Re\,S(b))\tag{4.4}$$

4.1.2 Model Description

The total cross section for a small $q\bar{q}$ dipole interacting with a dilute gluon field scales with the dipole's transverse area, the strong coupling constant, and the gluon density within the target.

$$\sigma_{q\bar{q}} = \frac{\pi^2}{N_c} r^2 \alpha_s(\mu^2) x g(x, \mu^2)$$
 (4.5)

where $xg(x, \mu^2)$ is the gluon density at some scale μ^2 . Now, consider a scenario where the gluon density within the target is significant. To analyze the interaction, we divide the target into thin longitudinal slices of thickness dz. The probability that a dipole, located at a given impact parameter b, traverses one such slice of the target without undergoing an

inelastic interaction is given by

$$P(b) = 1 - \frac{\pi^2}{N_c} r^2 \alpha_s(\mu^2) x g(x, \mu^2) \rho(b, z) dz$$
 (4.6)

Here $\rho(b,z)$ denotes the density of the gluons within a proton and is normalized to one

$$\int d^2bdz \rho(b,z) = 1 \tag{4.7}$$

By exponentiating this result, we obtain the total probability that the dipole passes through the entire proton without experiencing any inelastic interactions. This probability is expressed as an exponential suppression factor, accounting for the cumulative effect of multiple potential scatterings across all the thin slices of the target.

$$|S(b)|^{2} = exp\left(-\frac{\pi^{2}}{N_{c}}r^{2}\alpha_{s}(\mu^{2})xg(x,\mu^{2})T(b)\right)$$
(4.8)

Here T(b) is the thickness function

$$T(b) = \int_{-\infty}^{\infty} dz \rho(b, z) \tag{4.9}$$

To obtain the total cross section at a given impact parameter, we assume that the S-matrix element is predominantly real. Then the cross-section at a given impact parameter b is given by $2(1 - Re\ S(b))$ or

$$\frac{d\sigma_{q\bar{q}}}{d^2b} = 2\left[1 - \exp\left(-\frac{\pi^2}{2N_c}r^2\alpha_s(\mu^2)xg(x,\mu^2)T(b)\right)\right]$$
(4.10)

This is the Glauber-Mueller dipole cross section.

The dependence on the impact parameter is incorporated via the proton thickness function T(b), which is modeled as a Gaussian distribution and normalized to have an integral of one.

$$T(b) = \frac{1}{2\pi B_G} \exp\left(-b^2/2B_G\right)$$
 (4.11)

By examining the differential cross section as a function of the impact

parameter for various dipole sizes, it becomes evident that the total cross section described earlier starts to level off, or saturate. This saturation occurs at increasingly larger impact parameter values as the dipole size increases.

Rather than interpreting saturation as a phenomenon triggered below a specific energy threshold, it can also be understood in terms of dipole size: as the saturation scale grows, only smaller dipoles can effectively interact with the nucleus. This concept is depicted schematically in Figure 4.2 and is presented with more quantitative detail in Figure 4.3.

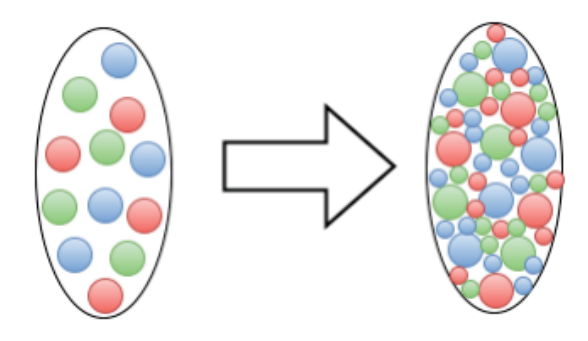


Figure 4.2: Schematic diagram showing that as energy increases, the gluon density inside the nucleon increases.

The gluon distribution function, $xg(x,\mu^2)$, is initialized at the scale $\mu_0^2=1~{\rm GeV^2}$ via

$$xg(x,\mu_0^2) = A_g x^{-\lambda_g} (1-x)^{5.6}$$
(4.12)

In the IP-Glasma model, the saturation radius r_s is defined as the dipole size at which the proton effectively spans one interaction length. This condition is implemented by setting the exponent in Equation (4.10) equal to 1/2. In other words, we define r_s such that:

$$\left(\frac{\pi^2}{2N_c}r^2\alpha_s(\mu^2)xg(x,\mu^2)T(b)\right)\bigg|_{r=r_s} = \frac{1}{2}$$
(4.13)

From there, the radius can be related to the saturation scale via

$$Q_{s,p}^2 = \frac{2}{r_s^2} \tag{4.14}$$

Plugging this into the dipole saturation cross section, we get

$$\frac{\pi^2}{2N_c}r^2\alpha_s(\mu^2)xg(x,\mu^2)T(b) = \frac{\pi^2}{N_cQ_{s,p}^2}\alpha_s(\mu^2)xg(x,\mu^2)T(b) = 1$$
 (4.15)

which, solving for Q_s ,

$$Q_{s,p}^{2} = \frac{\pi^{2}}{N_{c}} r^{2} \alpha_{s}(\mu^{2}) x g(x, \mu^{2}) T(b) \sim \frac{\rho_{g} \alpha_{s}(\mu^{2})}{A_{dipole}}$$
(4.16)

where the thickness function is a two-dimensional Gaussian that acts as the inverse of the spatial area of the dipole, $1/A_{dipole}$.

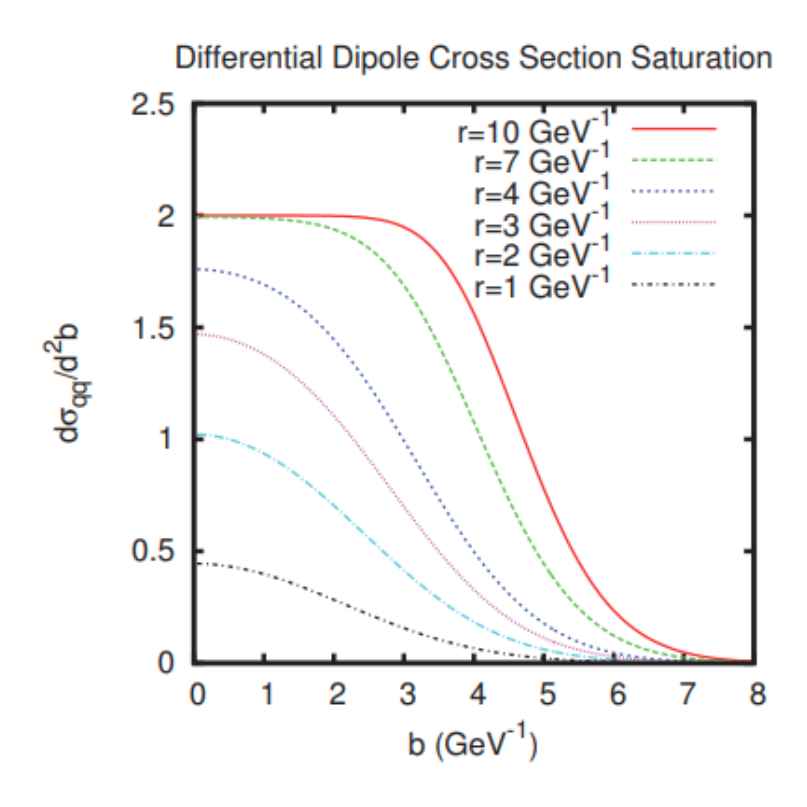


Figure 4.3: The differential dipole cross section as a function of impact parameter for different proton sizes [15].

Chapter 5

Result and Analysis

In this chapter, the analysis focuses on the two-particle correlation of neutral pions. The discussion begins with the basic kinematic plots depicting the transverse momentum of the neutral pions. We then see the di-pion correlation for the p-Pb system, for the differential multiplicity distribution, and the results with the saturation model are compared with the non-saturation one.

5.1 Transverse momentum distribution

In figure 5.1, the transverse momentum distribution of final state neutral pions is shown for saturation model and non saturation model. The center of mass energy of the collided particles, p-Pb is 5.02 TeV. From figure 5.1, it is observed that the JETSCAPE prediction with and without IP-Glasma matches well with each other.

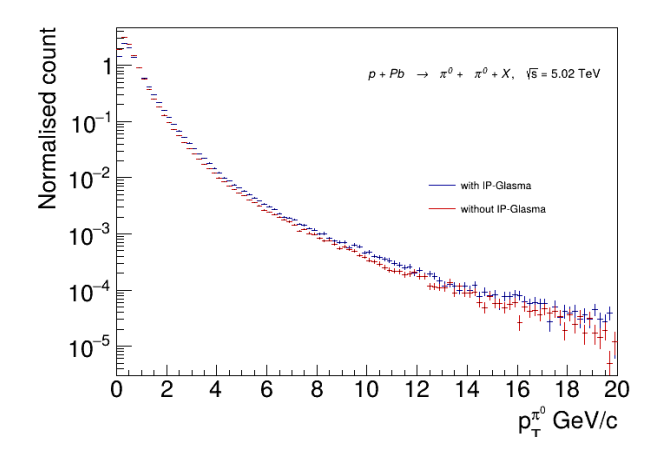


Figure 5.1: Normalized neutal-pion transverse momentum distribution from JETSCAPE.

5.2 Two-particle azimuthal correlation

In the two-particle azimuthal correlation, the correlation between a trigger neutral pion and an associated neutral pion is used. The basic idea is to make a correlation between a pair of neutral pions with high momentum imbalance. This study involves the measurement of relative angle $\Delta \phi$, where $\Delta \phi = \phi_{trig} - \phi_{assoc}$ is the difference in azimuthal angle. This function is sensitive to the momentum imbalance between the two hadrons.

The two-particle correlation function is defined as

$$C(\Delta\phi) = \frac{N_{pair}(\Delta\phi)}{N_{trig}} \tag{5.1}$$

where N_{pair} is the number of correlated pions and the N_{trig} is the number of trigger particles.

Figure 5.2, shows the $\Delta\phi$ correlation in the p-Pb system at $\sqrt{s}=5.02$ TeV, within the transverse momentum cut of, $p_T^{trig}>2$ GeV, and $1< p_T^{assoc}< p_T^{trig}$, and the pseudo-rapidity cut of $2.5< \eta < 5$. A dominant near-side peak ($\Delta\phi=0$) is observed, and a broad away-side peak ($\Delta\phi=\pi$) is seen. The away side shows no visible suppression in the away side. A similar study is done for differential multiplicity range, as shown in Figure 5.3, where multiplicity is divided into four different ranges. As seen in the STAR experiment results, a significant suppression is expected on the away side for high multiplicity events. The away-side peak for high multiplicity events shows a slight suppression, but is not statistically promising.

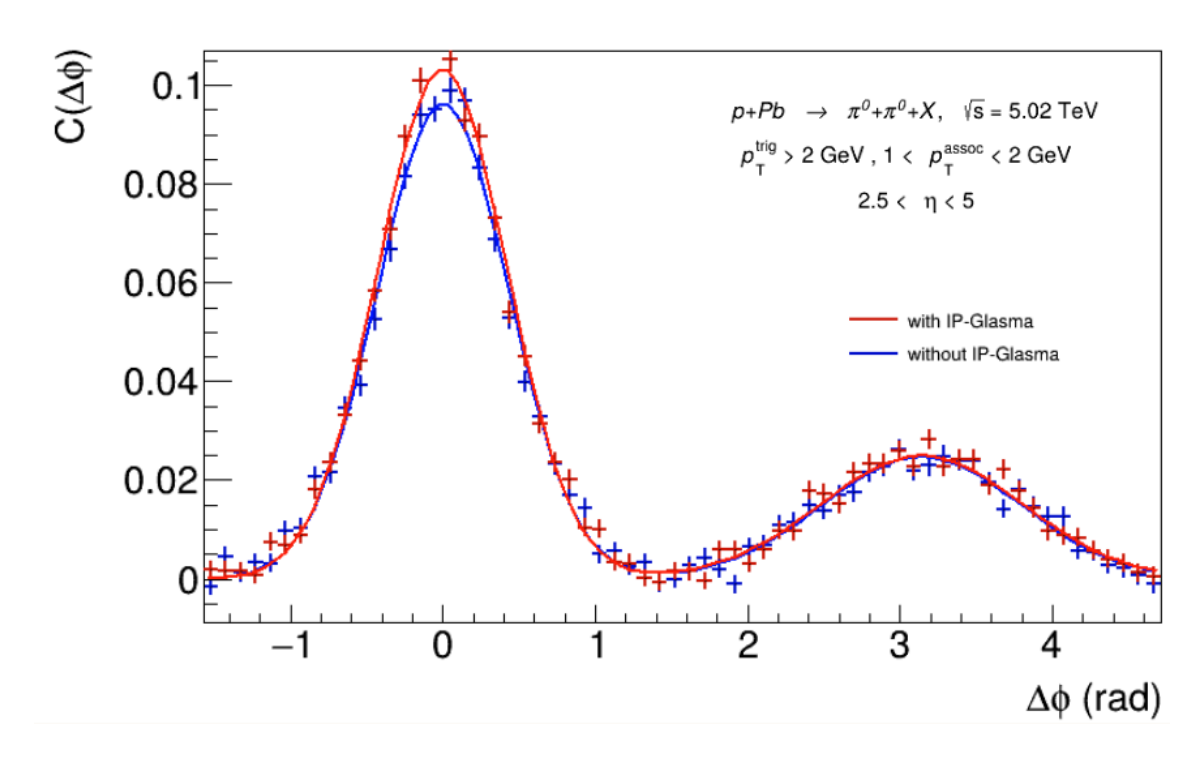


Figure 5.2: Azimuthal angle $(\Delta \phi)$ correlation between final state neutral-pions.

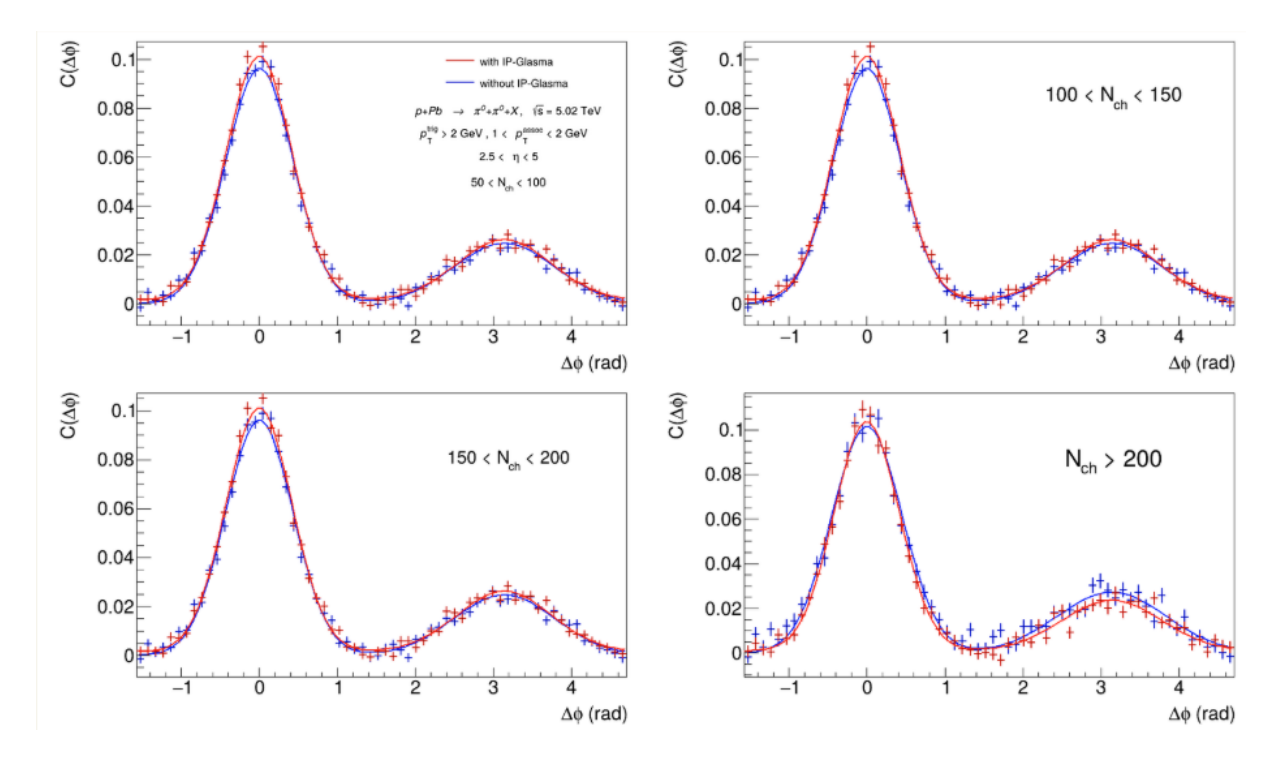


Figure 5.3: Azimuthal angle $(\Delta \phi)$ correlation between final state neutral-pions for different multiplicity ranges

Chapter 6

The EIC Experiment

The Electron-Ion Collider (EIC) will be the first collider to explore the inner workings of both protons and nuclei at high energies. It aims to answer fundamental questions about our visible world, such as the origin of nucleon spin, nucleon mass, and dense properties of the gluon systems. Using deep inelastic scattering (DIS) processes, the EIC's electron beam will probe protons and nuclei across a wide energy range of center of mass energy, $\sqrt{s} = 20$ to 140 GeV. This approach offers cleaner data compared to other collision types, enabling precise studies of strong interaction physics. The EIC White Paper outlines key aspects of its extensive physics program. The EIC's physics goal can be achieved by the study of three basic types of DIS processes:

- Inclusive DIS: $e + p/A \rightarrow e' + X$. For this reaction, it is imperative to measure the scattered electron, e', with high accuracy, as it is the primary particle used to determine the event's kinematic variables. Other final-state particles are not considered.
- Semi-inclusive DIS: $e + p/A \rightarrow e' + h^{\pm,0} + X$. This process involves measuring the scattered electron along with at least one identified hadron..
- Exclusive DIS: $e + p/A \rightarrow e' + p'/A' + \gamma/h^{\pm,0}/VM^1$. This process requires high-precision measurement of all particles in the event.

¹Vector Meson

At the EIC, all physics processes demand precise reconstruction of event and particle kinematics — including variables such as x, Q^2 , y, W^2 , p_T , z, ϕ , and θ . Key parameters like x, Q^2 , y, and W^2 can be determined from either the scattered electron or the hadronic final states. To cover the complete $x-Q^2$ plane across various center-of-mass energies and highly asymmetric beam energy configurations, the detector must accurately reconstruct events over an extensive rapidity range. Achieving this necessitates sufficient detector acceptance and resolution. Without effective coverage beyond the rapidity region $|\eta| > 2$, a considerable portion of the $x-Q^2$ phase space would be inaccessible at the EIC, highlighting the importance of the lepton and hadron end-caps. Figure 6.1 demonstrates the relationship between pseudo-rapidity, scattering angle, and the $x-Q^2$ phase space for the detector components near the interaction point. The central de-

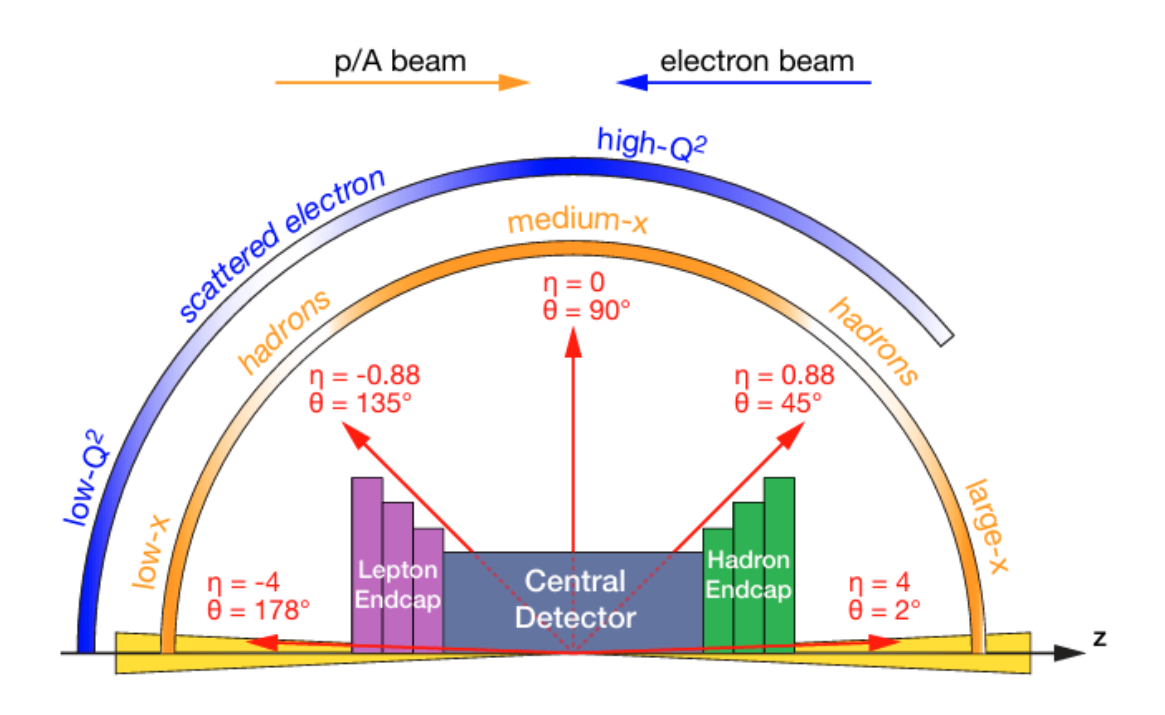


Figure 6.1: Schemaic layout of hadrons and the scattered lepton for different $x - Q^2$ distributed over the detector rapidity coverage [17].

tector, which covers roughly the region $|\eta| < 1$, is commonly called the barrel detector. The hadron and electron end-caps are often referred to as the forward and backward end-caps, respectively. This configuration is further complemented by very-small-angle detectors located farther from

the interaction point, known as the very forward and very backward detectors. However, geometrical acceptance is not the only limiting factor. For forward-moving high-energy particles, more significant constraints arise from the minimum detectable particle momentum, transverse momentum acceptance, and momentum measurement resolution. These challenges can be addressed by operating the central solenoid at different magnetic field strengths. Additionally, the EIC setup includes auxiliary systems such as the luminosity monitor and the lepton and hadron polarimeters, which are essential for the physics program.

6.1 Reference EIC detector

The rich physics potential of the EIC is closely linked to the experimental setup and the capabilities of its detectors. To realize the full scope of the EIC's scientific program, researchers will investigate three main types of processes: (i) inclusive, (ii) semi-inclusive, and (iii) exclusive interactions. These studies will involve collisions between electrons and either light or heavy nuclei, utilizing polarized beams for both electrons and light nuclei, and will cover a broad spectrum of center-of-mass energies.

A conceptual design for the central detector closely aligned with the physics objectives is shown as a 3D representation in Figure 6.2 and as a 2D schematic in Figure 6.3. Figure 6.4 highlights the layout of the very forward detectors. The design is based on the following key features.

The central detector is engineered to provide coverage across a wide pseudo-rapidity interval $-4 < \eta < 4$, with full instrumentation within the core region of $|\eta| < 3.5$. This extensive acceptance is specifically tailored to meet the demands of a diverse set of physics studies, including inclusive and semi-inclusive measurements, jet reconstruction, and hadron spectroscopy. These processes require the ability to detect particles over a broad angular range with high precision.

To achieve nearly complete event reconstruction, referred to as detector hermeticity, and to enable the identification of particles scattered at small

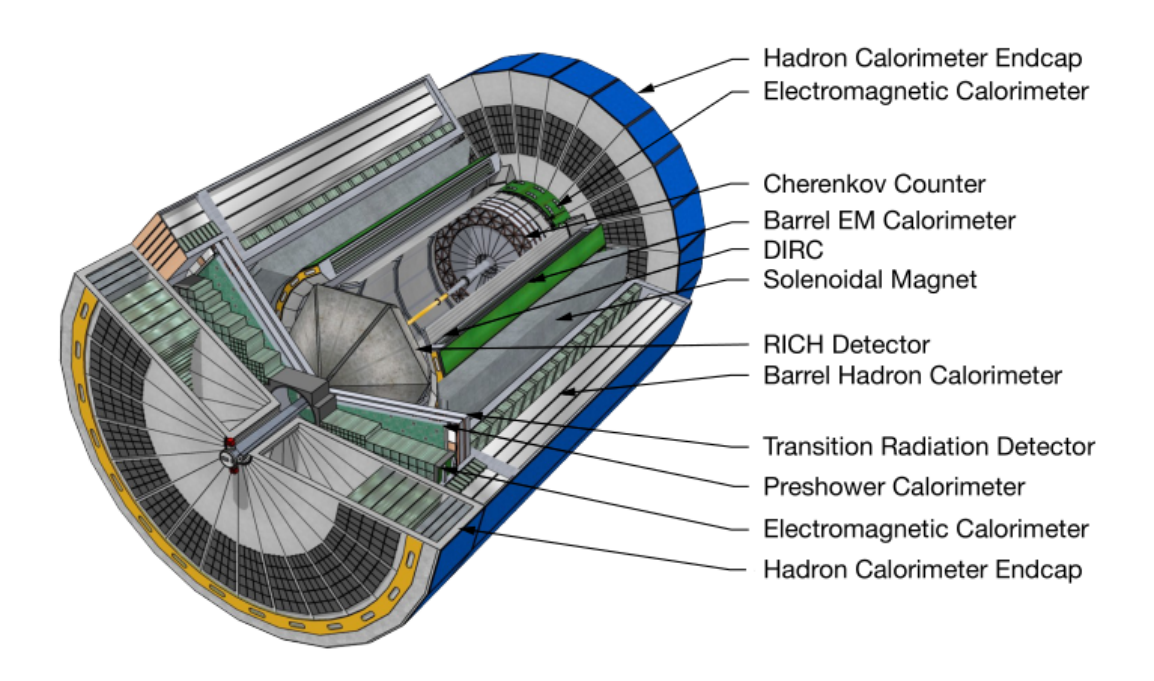


Figure 6.2: 3D model of EIC detector design[18].

angles, particularly those relevant for exclusive and diffractive processes, the central detector is augmented with specialized very forward and backward detection systems. These additional components are essential for tagging leading particles and detecting remnants of the ion or electron beams, which are key signatures in many targeted physics channels.

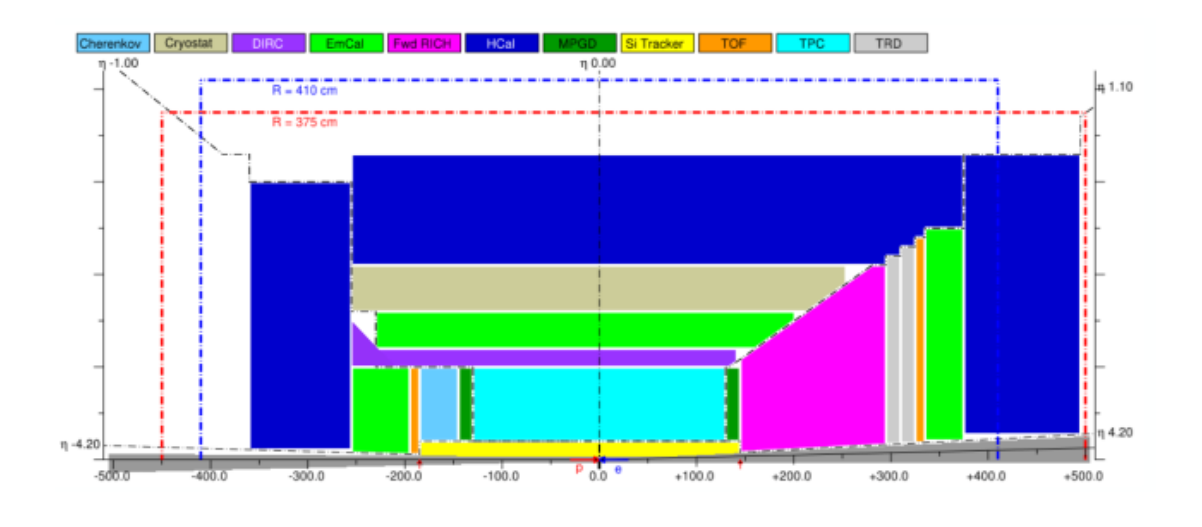


Figure 6.3: A 2D schematic of an EIC detector layout[18].

The design of the central detector is guided by the geometrical characteristics of collision events and the specific scientific objectives of the

EIC. The detector must fulfill several critical performance criteria. These include:

- 1. High-resolution tracking and momentum measurement capabilities to accurately reconstruct charged particle trajectories;
- 2. Reliable electron identification to distinguish electrons from the abundant background of hadrons and photons;
- 3. Effective hadron identification over a wide momentum range to separate different species such as pions, kaons, and protons;
- 4. Precise jet energy measurements to analyze the structure and dynamics of hadronic final states;
- 5. Compact and optimized physical dimensions that are consistent with the spatial constraints and interaction region design of the collider.

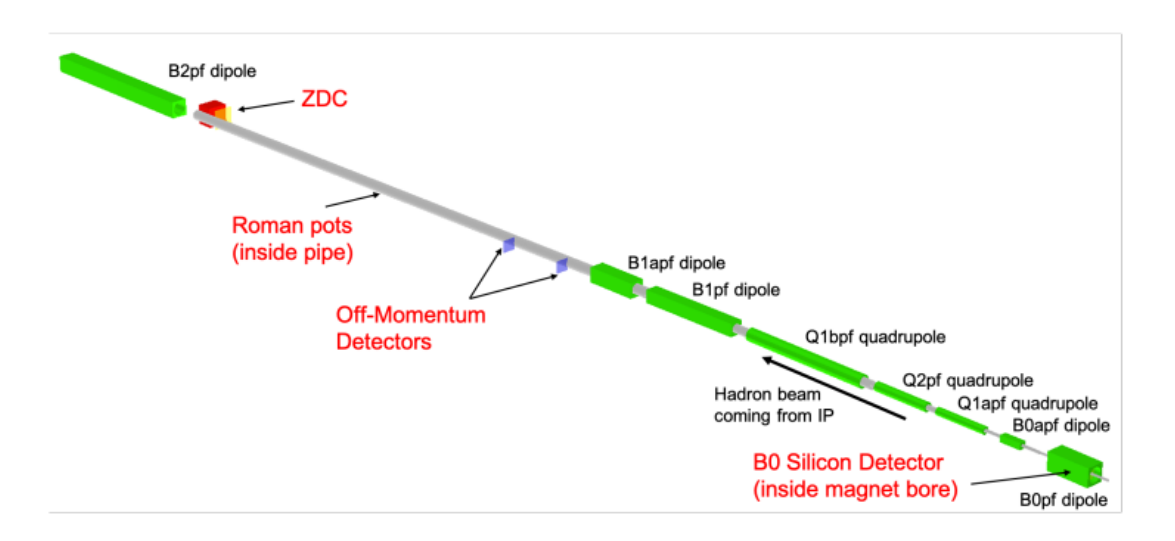


Figure 6.4: A GEANT4 visualization depicts the far-forward hadron beam magnets in green, along with a simplified illustration of the beam pipe and the four detector subsystems that are currently part of the reference detector configuration[18].

Together, these features ensure that the central detector can support the full breadth of the EIC's physics program, providing the necessary precision and versatility for cutting-edge measurements. In Figure 6.5, we have a view of the first detector of EIC, called ePIC. It is a collection of many sub-detectors. It has a 1.7 Tesla superconducting magnet for curving the trajectories of the charged particles created in collisions, high-precision silicon detectors for tracking particle trajectories in the magnetic field, precise calorimeters for measuring the energy of the particles, and excellent particle identification detectors. This experimental facility is still in the development phase and the detector is also virtual. So

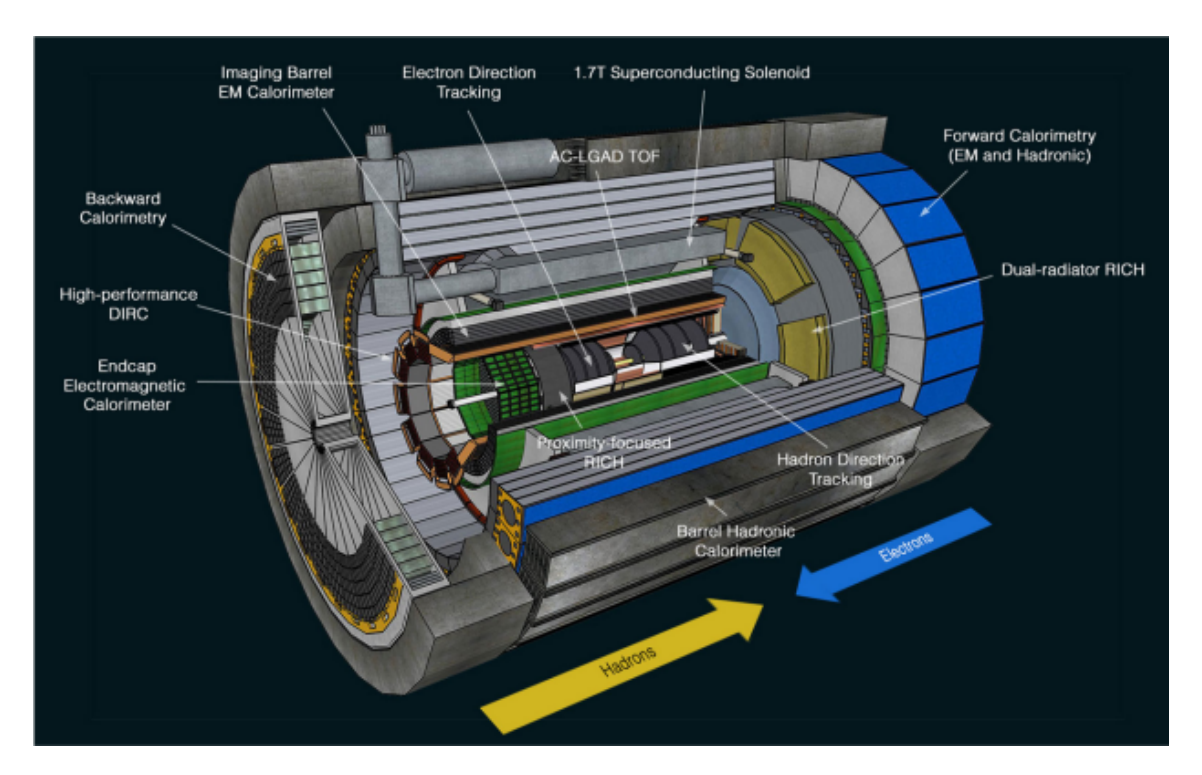


Figure 6.5: 3D schematic of an ePIC detector design[17]

the task that we are doing is to study the resolution and efficiency of the detector so that we can optimize it for better performance. This kind of study is incredibly valuable in the development phase of any experimental facility. This allows us to explore various design parameters, optimize performance, and anticipate potential challenges before committing to physical construction. The process is as follows:

We've obtained data from e-p collisions simulated using the event generator PYTHIA. This data is then passed through our virtual detector setup, yielding output that includes hit positions, energy, momentum, and other relevant information. By comparing the kinematics of the particles generated by PYTHIA with those detected or reconstructed by the virtual detector, we can assess the performance of our detector.

Efficiency is defined as

Efficiency =
$$\frac{\text{Reconstructed }(p_T, \eta, \phi, ...)}{\text{Generated }(p_T, \eta, \phi, ...)}$$
(6.1)

Resolution is given by,

Resolution =
$$\frac{\text{Reconstructed }(p_T, \eta, \phi, ...) - \text{Generated }(p_T, \eta, \phi, ...)}{\text{Generated }(p_T, \eta, \phi, ...)}$$
(6.2)

6.2 Track reconstruction method

Modern particle tracking systems employ two distinct reconstruction approaches to handle different experimental requirements. These methods balance computational efficiency with physical accuracy through complementary strategies. Truth-seeded reconstruction is designed as an idealized approach, where every final-state charged particle generated in the simulation is used to create a track seed based on its true physical parameters. Specifically, the true charge, momentum (q/p), polar and azimuthal angles (θ, ϕ) , and the exact generation vertex are employed directly to initialize the seed. There is also an option to apply smearing to these initial parameters to mimic detector resolution effects, but fundamentally, the method assumes perfect knowledge of the particle's trajectory at the outset. The workflow proceeds by passing these seeds into a combinatorial Kalman filter (CKF) for track finding and fitting, followed by geometric matching between reconstructed tracks and generated particles. This approach provides a benchmark for the best possible tracking performance, as it is unaffected by detector inefficiencies or ambiguities in hit association.

In contrast, real-seeded reconstruction reflects the practical realities of experimental data analysis. Here, seeds are generated using the ACTS orthogonal seeder, which identifies triplets of space points-clusters of hits in the silicon detectors-that are consistent with the expected trajectory of

a charged particle moving in a uniform magnetic field. The seed finder and filter are highly configurable, with parameters set to define the search region in radius and z, the allowed angular range, and minimum transverse momentum, among others. Once a seed is formed, the seed space points are fit to extract the initial track parameters (charge, q/p, θ , ϕ , and position), and these are then passed to the CKF for full track finding and fitting. Real-seeded reconstruction must contend with the possibility of seed duplication, as multiple combinations of space points can correspond to the same underlying particle, especially in regions where a particle crosses many detector layers. Ambiguity resolution is therefore an essential step, ensuring that only the best candidate track is retained for each particle.

Both methods use the same downstream tracking algorithms, with the main distinction lying in how the initial seeds are formed. Truth-seeded reconstruction provides an idealized reference for algorithm development and detector benchmarking, while real-seeded reconstruction is essential for realistic performance estimates and ultimately for analyzing experimental data. Ongoing developments include refining the seed finder for large-|z| vertices, implementing hit-level matching between tracks and generated particles, and improving ambiguity resolution to further enhance the fidelity and efficiency of the reconstruction process.

6.3 Efficiency of charged pions

In Fig. 6.6, we observe the efficiency distribution represented by the ratio of the reconstructed p_T to the generated p_T for the truth-seeded track. The efficiency plot is prominently centered at 1. Similarly, in Fig. 6.7, we observe the efficiency distribution represented by the ratio of the reconstructed p_T to the generated p_T for the real-seeded track. The efficiency plot is prominently mean around 1. In Fig. 6.8, we observe the efficiency distribution represented by the ratio of the reconstructed η to the generated η for the truth-seeded track, with the efficiency plot prominently mean around 0.85, and for the real-seeded track, with the efficiency plot

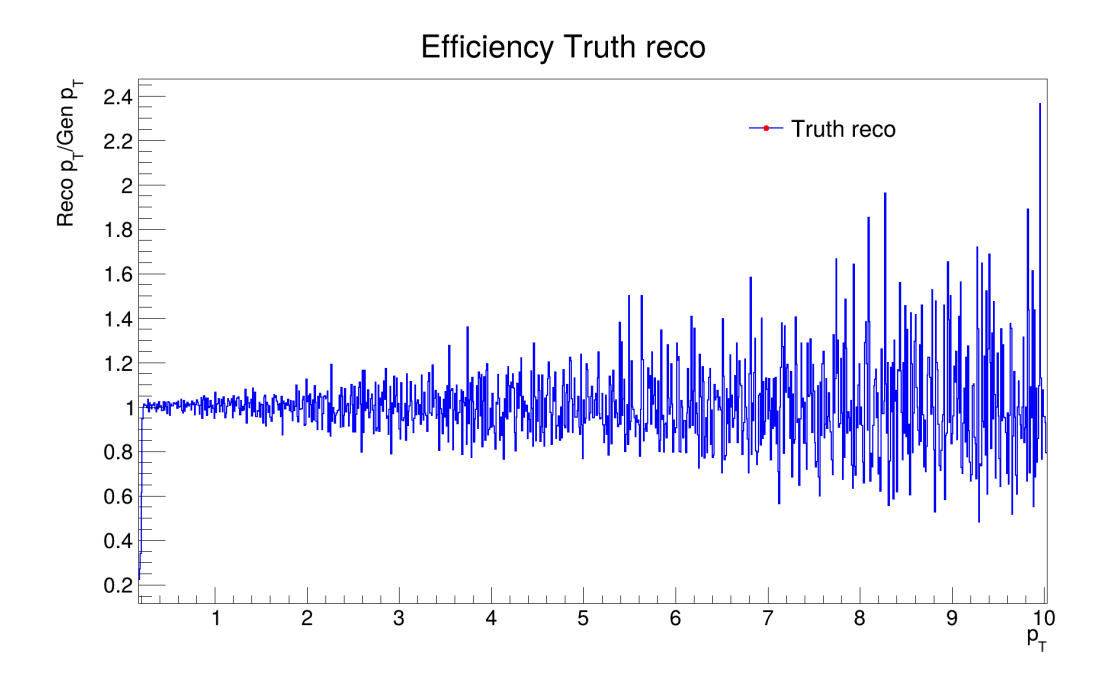


Figure 6.6: Variation of efficiency with transverse momentum (p_T) of charged pions for truth-seeded track

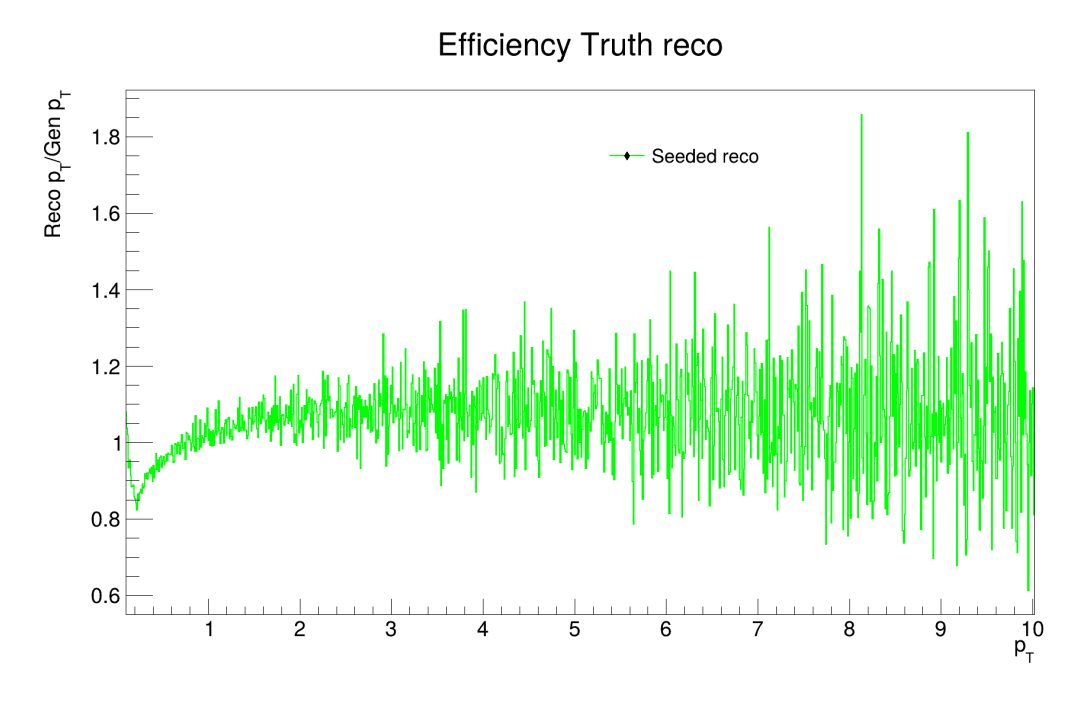


Figure 6.7: Variation of efficiency with transverse momentum (p_T) of charged pions for truth-seeded track

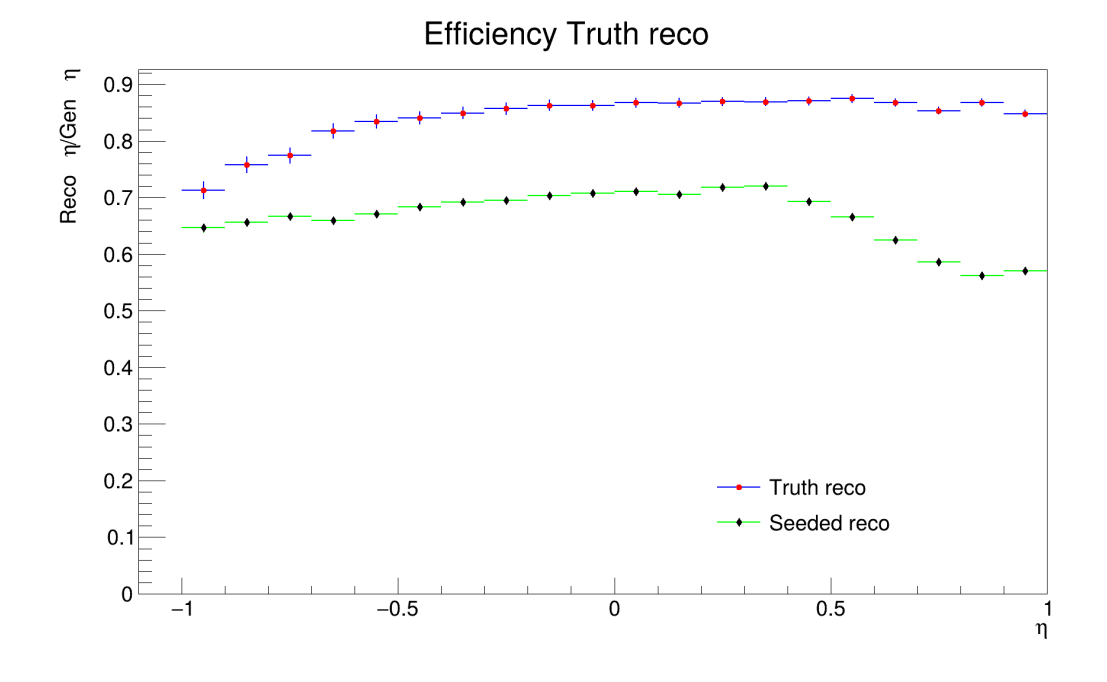


Figure 6.8: Variation of efficiency with pseudo-rapidity (η) of charged pions for truth-seeded track

prominently mean around 0.7.

6.4 Momentum resolution of charged pions

6.4.1 Momentum resolution for truth seeded particles

This section will show the momentum resolution of charged pions with varying η ranges. Figure 6.9 shows the momentum resolution of charged pion vs generated p_T in the mid eta range $|\eta| < 1$. The resolution is nicely centered around zero, showing good resolution. In fig. 6.10 and 6.11, we have the projection of 2D-histogram onto the y-axis, for different p_T ranges as shown in the figures and these distributions are fitted with double Gaussian² function and sigma (σ) of each distribution for the particular p_T range is calculated. Sigma (σ) in each p_T interval shows deviation up to 0.7%, see fig. 6.12. The effective sigma of the double Gaussian function is calculated using

$$\sigma = \sqrt{\frac{A_1 \sigma_1^2 + A_2 \sigma_2^2}{A_1 + A_2}} \tag{6.3}$$

²Double Gaussian function is the sum of two Gaussian function

here σ_1 and σ_2 are the standard deviation of each Gaussian and A_1 and

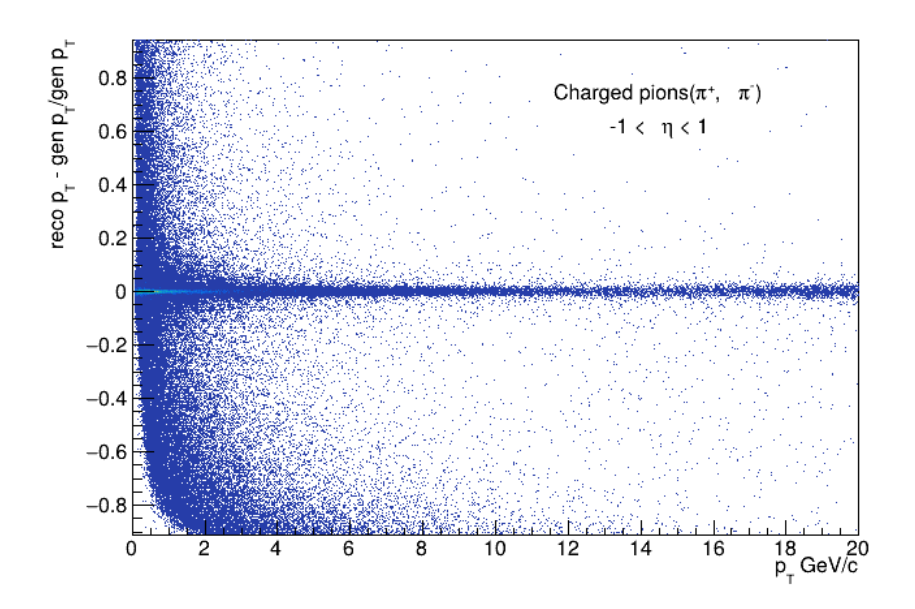


Figure 6.9: Momentum resolution of charged pions in $|\eta| < 1$ range.

 A_2 is the amplitude of each Gaussian function.

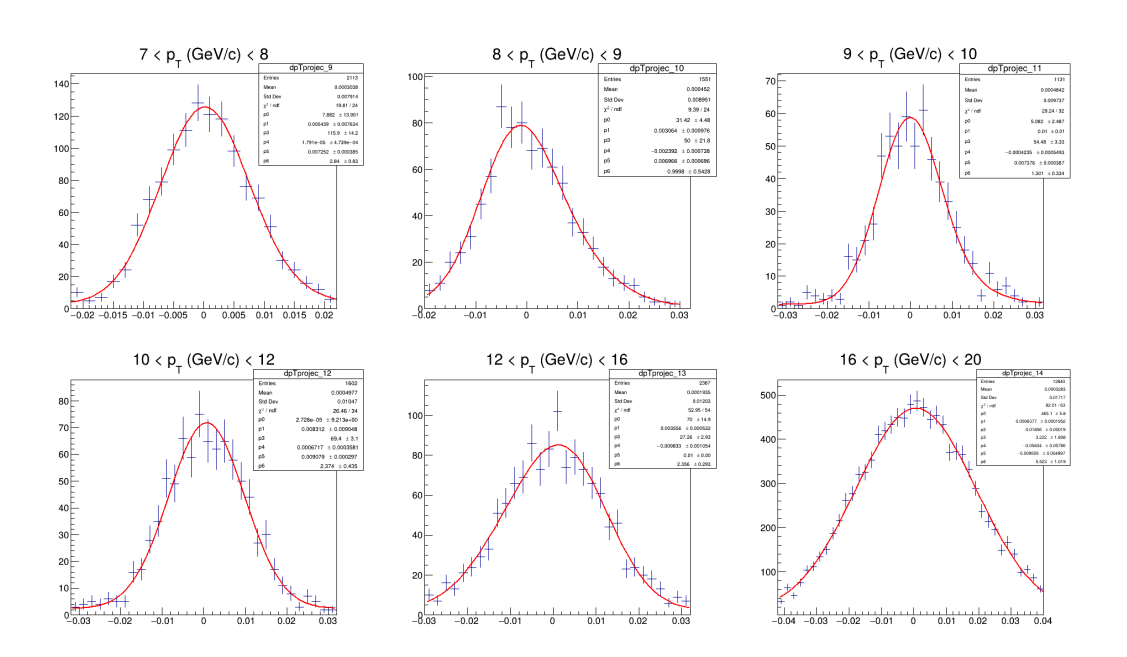


Figure 6.10: Resolution across various p_T ranges, fitted with double Gaussian function

Similar studies are done for other η ranges as well, as shown in Figure 6.13.

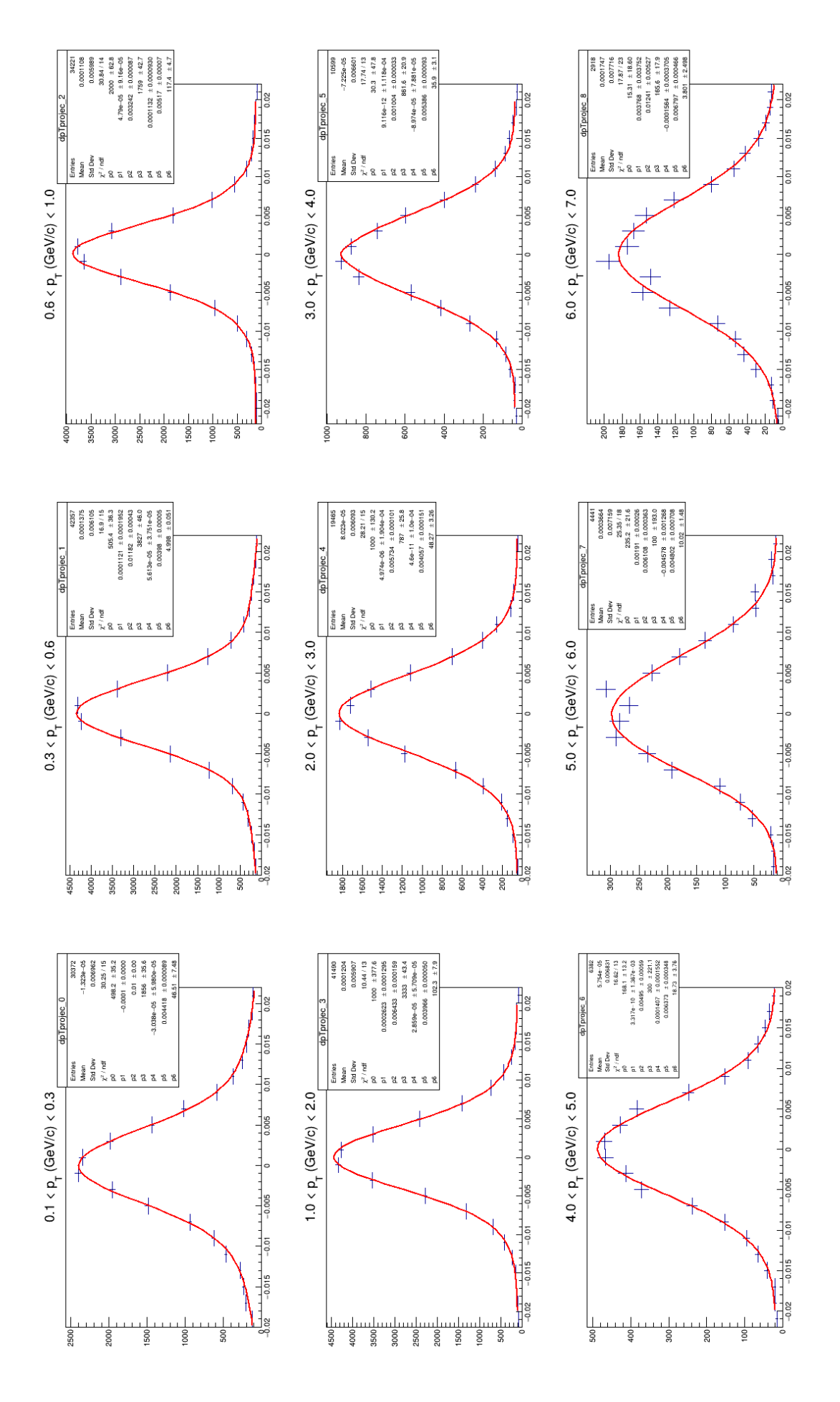


Figure 6.11: Resolution across various p_T ranges, fitted with double Gaussian function

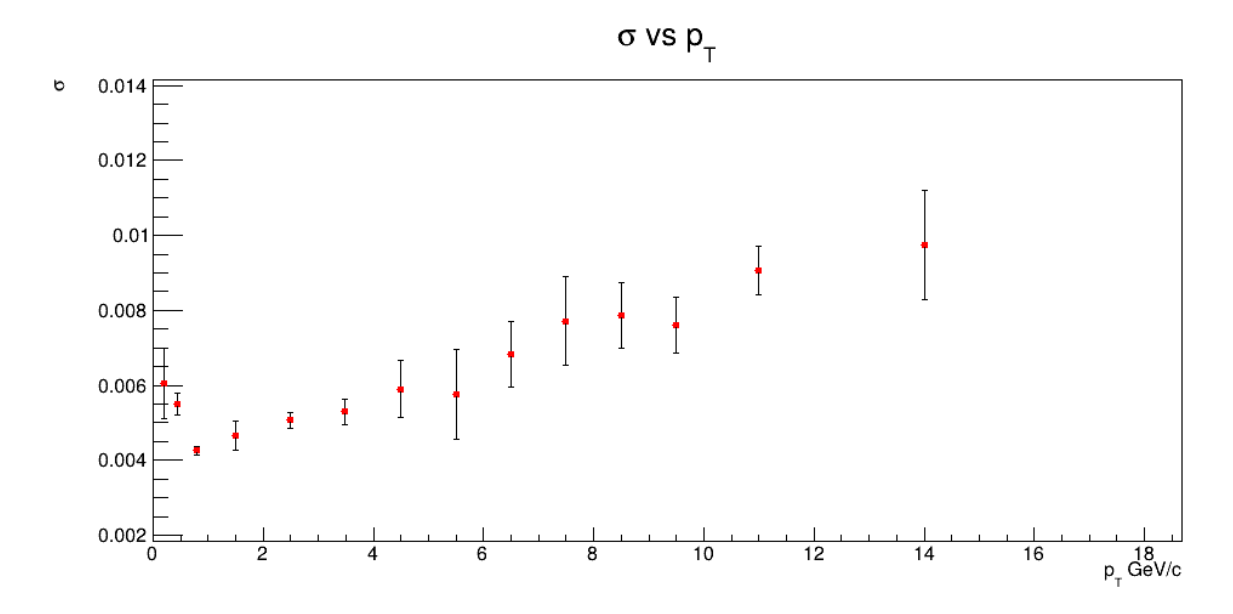


Figure 6.12: Sigma (σ) vs p_T for charged pion at $|\eta| < 1$

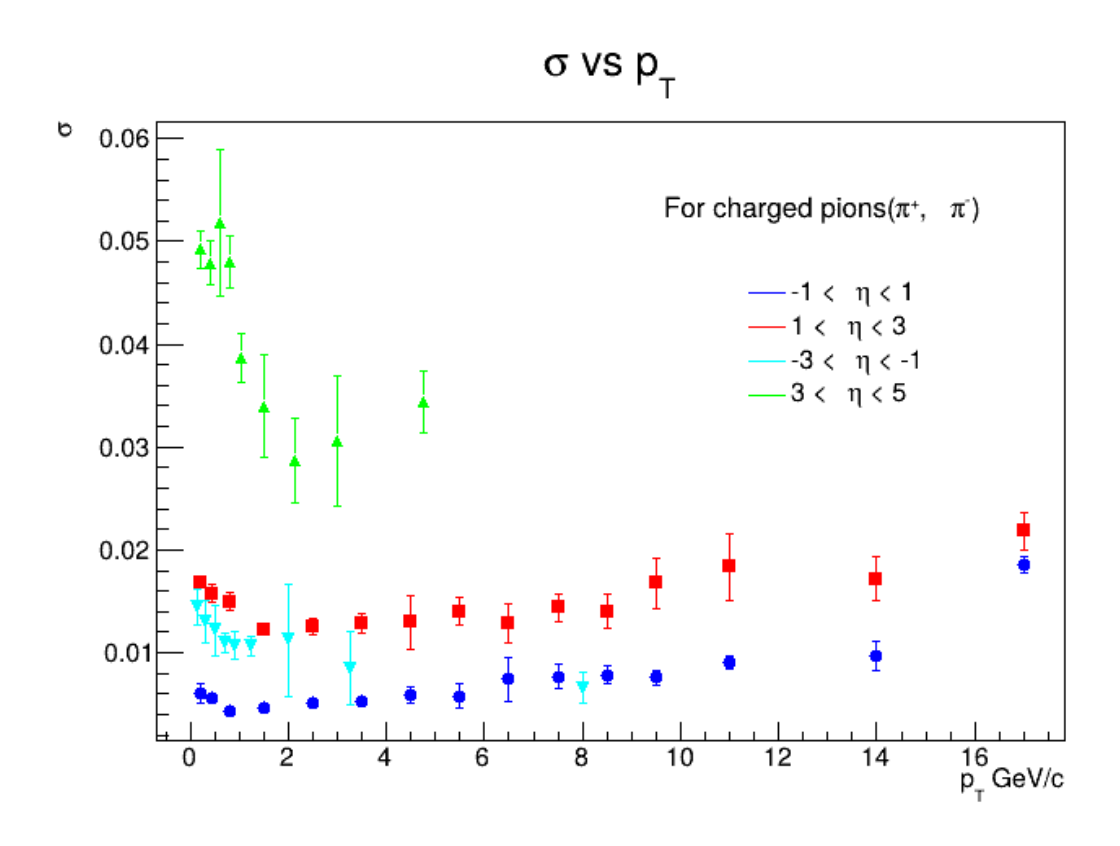


Figure 6.13: Sigma (σ) vs p_T for charged pion at different η ranges.

6.4.2 Momentum resolution for real seeded particles

A similar study was done for the real-seeded data as well. Figure 6.14 shows the momentum resolution of charged pions vs generated p_T in the positive forward eta range $1 < \eta < 3$ for the real-seeded branch. The resolution is nicely centered around zero, showing good resolution. Figure 6.15 and 6.16 shows the projection of the 2D histogram onto the y-axis for different p_T ranges as in the figure, and these distribution is again fitted with a double Gaussian function, and the sigma (σ) of each distribution for the particular p_T range is calculated. Sigma (σ) in each p_T interval shows deviation up to 1.5%, see Fig. 6.17. The effective p_T of the double Gaussian is calculated using equation 6.3.

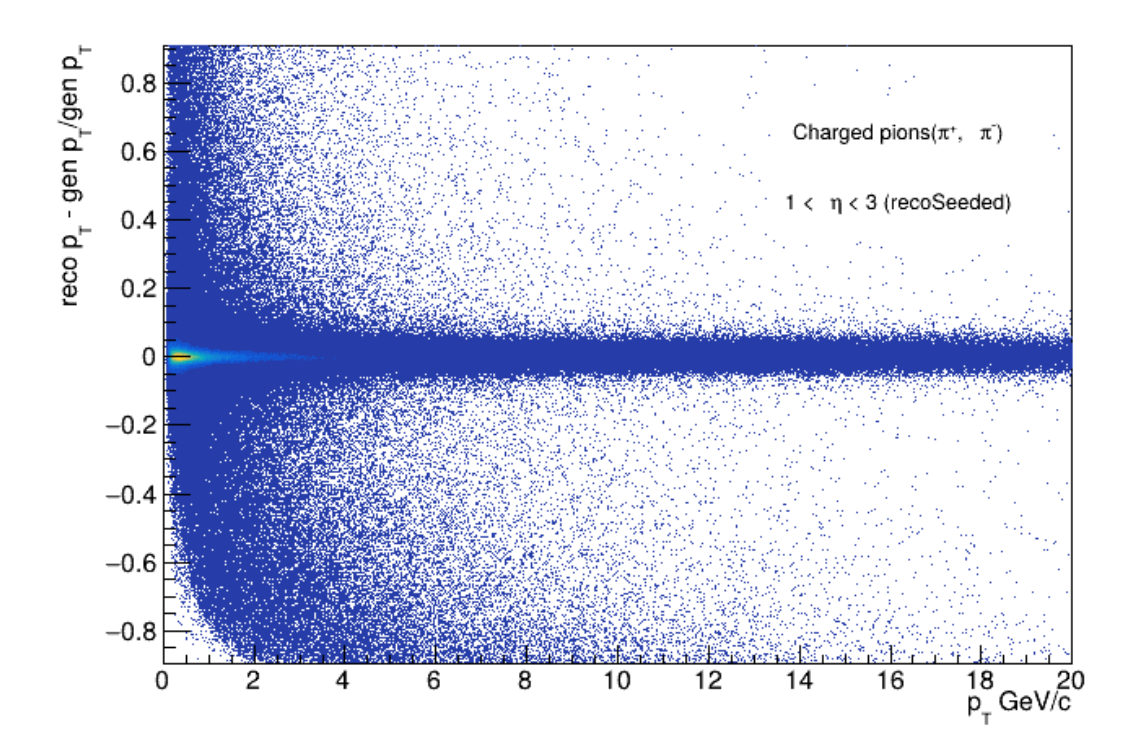


Figure 6.14: Momentum resolution of charged pions in $1 < \eta < 3$ range for real-seeded branch

We find the σ vs p_T for other η ranges as well, see fig. 6.18 and then compare the results for the truth-seeded and real-seeded data, see Fig. 6.19.

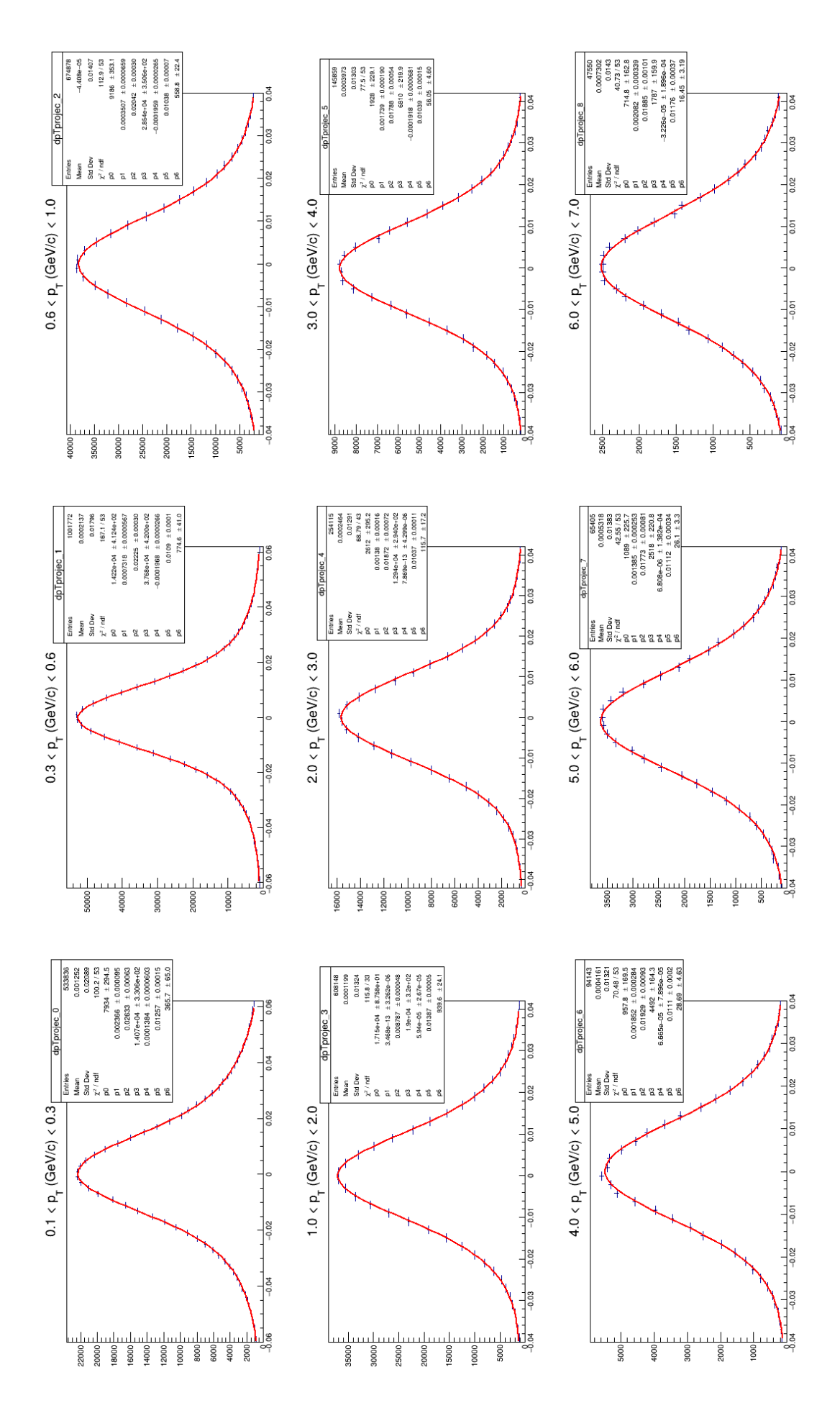


Figure 6.15: Resolution across various p_T ranges, fitted with double Gaussian function

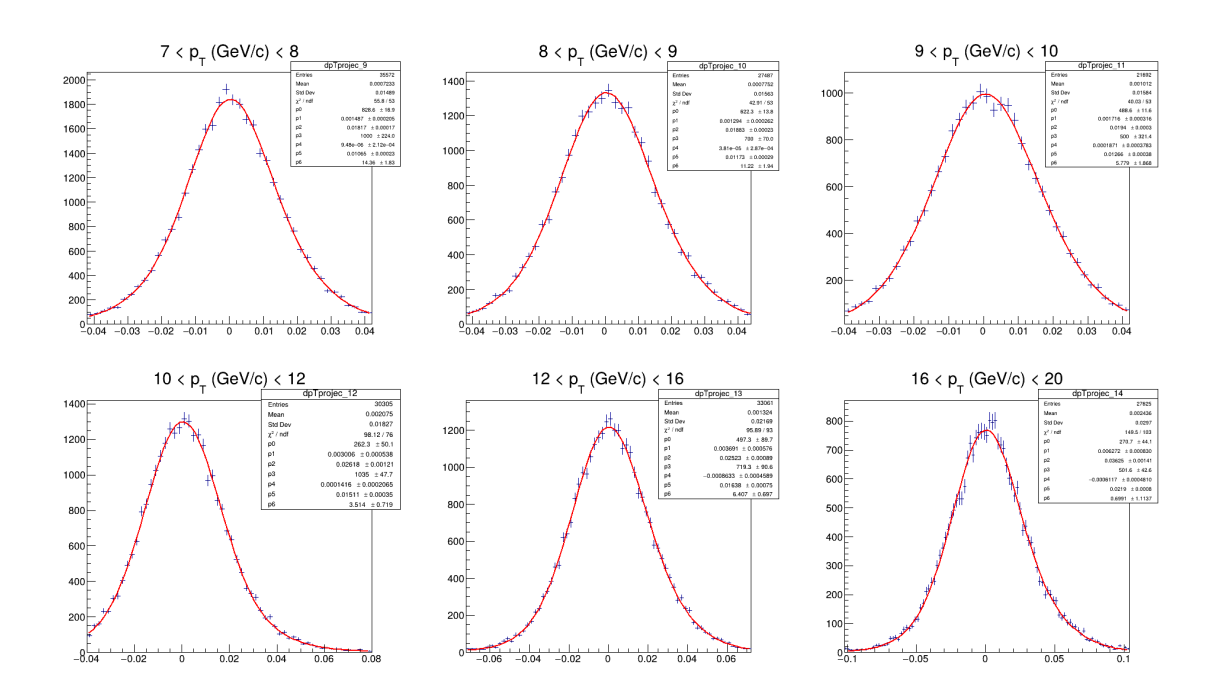


Figure 6.16: Resolution across various p_T ranges, fitted with double Gaussian function

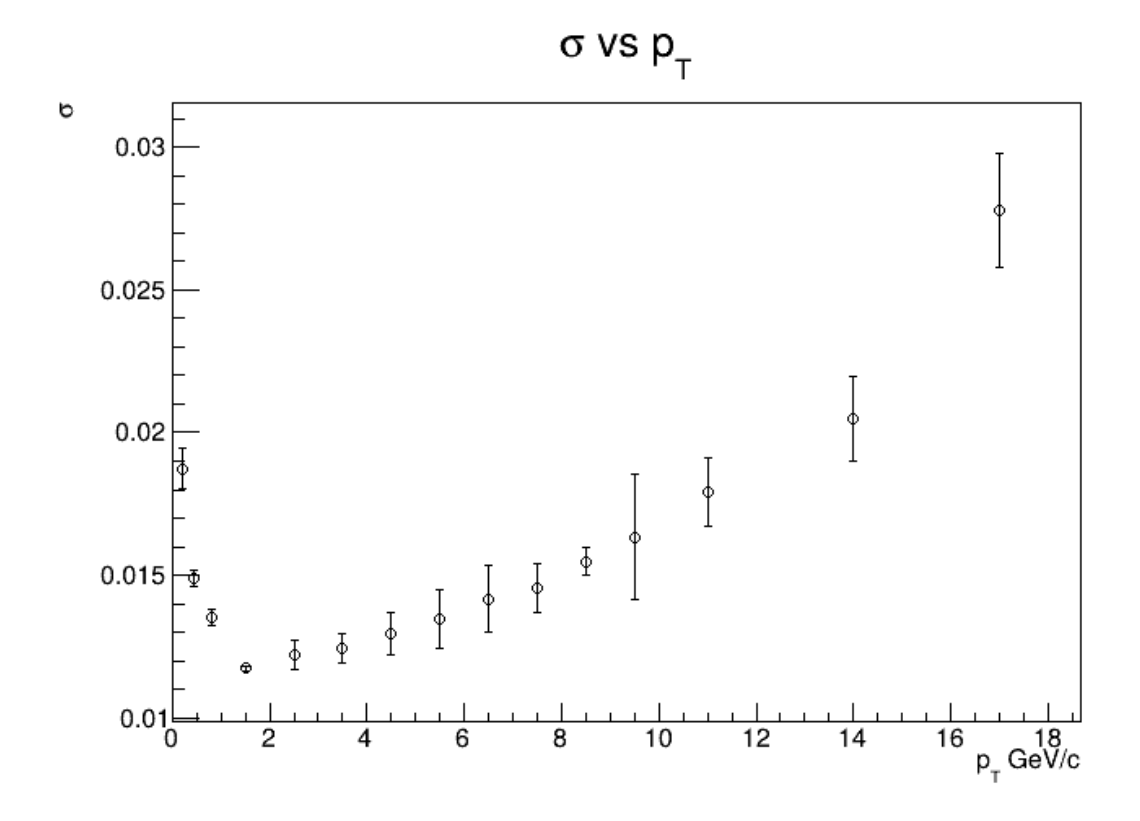


Figure 6.17: σ vs p_T for charged pions at $1 < \eta < 3$

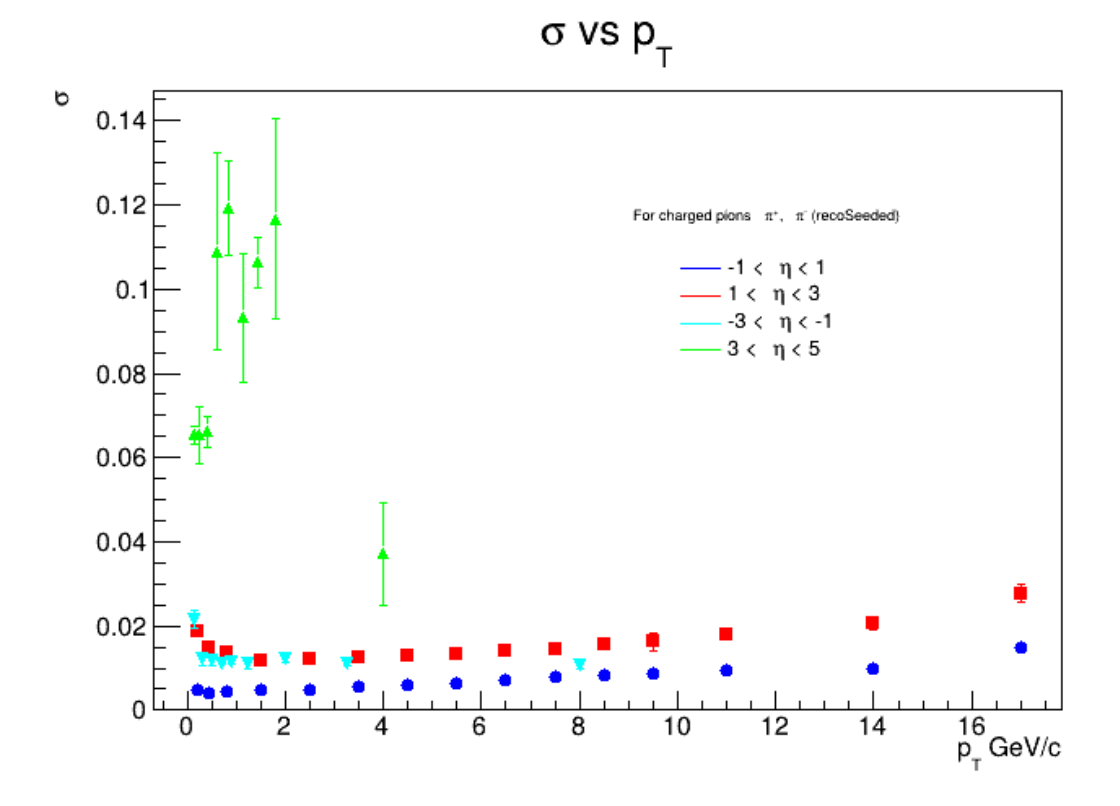


Figure 6.18: Sigma (σ) vs p_T for charged pion at different η range.

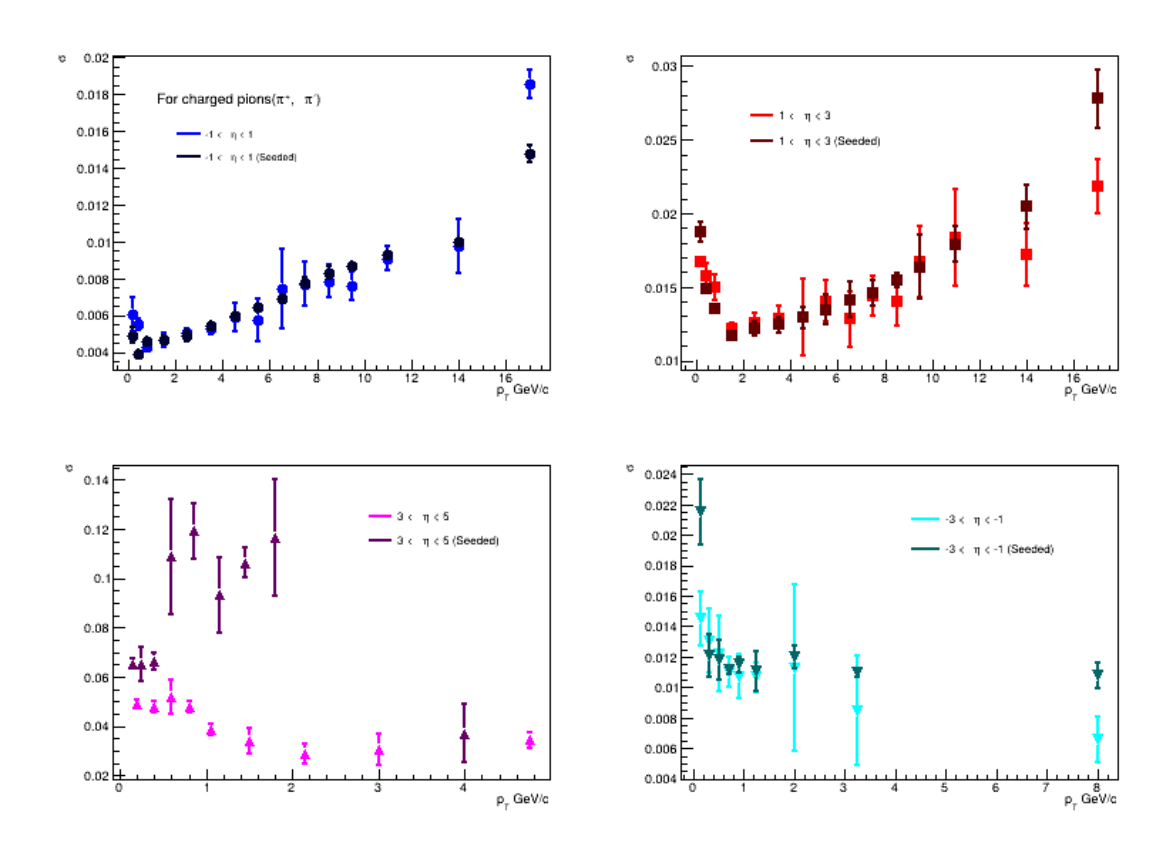


Figure 6.19: Comparison between truth seeded sigma (σ) vs p_T and real seeded sigma (σ) vs p_T for charged pion at different η ranges.

Chapter 7

Summary

This thesis presents a comprehensive investigation into gluon saturation phenomena in quantum chromodynamics (QCD) through di-hadron correlation studies and evaluates the efficiency and resolution of the ePIC detector for the forthcoming Electron-Ion Collider (EIC). Gluon saturation, a non-linear QCD effect, is expected to occur at high energies (small Bjorken-x), where gluon densities in protons and nuclei become so large that recombination processes counterbalance gluon splitting. This regime, described by the Color Glass Condensate (CGC) framework, is of fundamental interest for understanding the collective behavior of partons in dense nuclear matter.

A central focus of the thesis is the use of di-hadron (two-particle) azimuthal correlations as a sensitive probe of gluon saturation. In high-energy proton-nucleus (p+A) and deuteron-gold (d+Au) collisions, the typical back-to-back correlation of hadron pairs-characterized by a peak at azimuthal angle difference $\Delta\phi\approx\pi$ -becomes suppressed and broadened in the presence of saturation. This decorrelation results from multiple scatterings and gluon recombination in the dense nuclear medium, leading to a significant modification of the away-side peak in azimuthal distributions. Experimental results from the STAR experiment at RHIC, utilizing forward rapidity measurements and upgraded detector systems, provide strong evidence for this suppression in central d+Au collisions. These findings are consistent with CGC predictions and are not reproduced by

conventional models such as PYTHIA or HIJING, which do not incorporate saturation effects. The thesis demonstrates that such di-hadron correlation measurements are among the most direct and sensitive methods to access the underlying gluon dynamics and to constrain saturation models.

The theoretical framework underpinning these studies is detailed through the discussion of the IP-Sat and IP-Glasma models, which simulate the initial conditions of heavy-ion collisions by incorporating impact-parameterdependent gluon saturation and classical Yang-Mills dynamics. The thesis describes how these models are used to calculate color charge configurations, gauge field evolution, and the resulting energy density profiles essential for hydrodynamic simulations. The saturation scale, Q_s , emerges as a key parameter, growing with both nuclear size and collision energy, and delineating the transition from dilute to saturated gluon regimes.

In addition to the phenomenological and experimental analysis, the thesis evaluates the performance of the ePIC detector, the reference detector for the EIC. The EIC is designed to deliver unprecedented access to the small-x regime, enabling high-precision studies of nucleon and nuclear structure via deep inelastic scattering (DIS). The thesis outlines the kinematic variables central to DIS-such as Bjorken-x, photon virtuality Q^2 , rapidity, and transverse momentum-and describes the use of Monte Carlo event generators (notably JETSCAPE) to simulate collision events, incorporating both initial state models and hydrodynamic evolution.

The detector performance study centers on the reconstruction efficiency and momentum resolution for charged pions, employing both truth-seeded (idealized) and real-seeded (experimentally realistic) tracking algorithms. Efficiency is quantified as the ratio of reconstructed to generated kinematic variables, with results showing high efficiency (centered around unity for transverse momentum, slightly lower for pseudo-rapidity). Momentum resolution is assessed using double Gaussian fits across various momentum and rapidity ranges, revealing that the detector achieves good resolution, with deviations typically below 1%. These findings indicate that the ePIC de-

tector design is well-suited for the EIC's ambitious physics goals, offering the necessary precision and coverage to explore gluon saturation and other key QCD phenomena.

In summary, this thesis provides both a theoretical and experimental foundation for the study of gluon saturation using di-hadron correlations and establishes the readiness of the ePIC detector for high-precision measurements at the EIC. The results pave the way for future investigations that will deepen our understanding of QCD in the high-density regime and address fundamental questions about the structure of matter.

Appendix A

JETSCAPE setting for saturation effects

```
2 <?xml version="1.0"?>
4 <jetscape>
    <vlevel> 0 </vlevel>
    <nEvents> 1000000 </nEvents>
    <setReuseHydro> true </setReuseHydro>
    <nReuseHydro> 10000 </nReuseHydro>
11
    <outputFilename>music_ipglasma_5TeV_pTHat_2_Ev100k</outputFilename>
12
    <JetScapeWriterAscii> on </JetScapeWriterAscii>
    <JetScapeWriterFinalStatePartonsAscii>
14
15
    </JetScapeWriterFinalStatePartonsAscii>
    <JetScapeWriterFinalStateHadronsAscii>
18
    </JetScapeWriterFinalStateHadronsAscii>
19
    <Random>
21
      <seed>0</seed>
    </Random>
    <!-- Inital State Module -->
25
     <IS>
          <!-- <Trento> </Tremto>-->
          <IPGlasma> </IPGlasma>
28
      </IS>
    <!-- Hard Process -->
```

```
<Hard>
      <PythiaGun>
33
         <FSR_on>1</FSR_on>
         <pTHatMin>2</pTHatMin>
35
         <pTHatMax>1000</pTHatMax>
36
         <eCM>5020</eCM>
         <LinesToRead>
39
           HardQCD:all = on
           PDF:useHardNPDFA=on
           PDF:useHardNPDFB=on
42
           PDF:nPDFSetA=1
           PDF:nPDFSetB=1
           PDF:nPDFBeamA = 2212
45
           PDF:nPDFBeamB = 100822080
46
         </LinesToRead>
47
      </PythiaGun>
48
    </Hard>
49
50
    <!--Preequilibrium Dynamics Module -->
51
      <Pre><Prequilibrium>
52
           <!--<NullPreDynamics> </NullPreDynamics>-->
53
           <Glasma> </Glasma>
54
      </Preequilibrium>
56
    <!-- Hydro
                Module -->
57
      <Hydro>
           <MUSIC>
               <Initial_time_tau_0>0.4</Initial_time_tau_0>
60
               <freezeout_temperature>0.15</freezeout_temperature>
61
           </MUSIC>
      </Hydro>
63
64
    <!--Eloss Modules -->
      <Eloss>
66
           <Matter>
67
               <in_vac> 0 </in_vac>
           </Matter>
70
           <Lbt>
               <name> Lbt </name>
               <in_vac> 0 </in_vac>
73
           </Lbt>
74
      </Eloss>
75
77
      <SoftParticlization>
           <!-- iSpectraSampler -->
```

```
<iSS>
79
               <hydro_mode>1</hydro_mode>
80
               <!-- hadron species list 0: PDG 2005; 1: UrQMD; 2: SMASH --
               <afterburner_type>1</afterburner_type>
82
           </iSS>
       </SoftParticlization>
84
85
      <!-- Hadronic Afterburner -->
      <Afterburner>
           <output_only_final_state_hadrons>1
      output_only_final_state_hadrons>
           <!-- SMASH -->
89
           <SMASH>
               <name>SMASH</name>
91
           </SMASH>
       </Afterburner>
94
95
      <!-- Jet Hadronization Module -->
       <JetHadronization>
           <name>colorless</name>
98
           <eCMforHadronization>2510</eCMforHadronization> <!-- Default
      2510-->
           <pythia_decays>off</pythia_decays>
100
       <!-- lets the particles given to pythia decay-->
101
       </JetHadronization>
102
104 </jetscape>
```

Appendix B

Azimuthal angle correlation

```
void Corre_trig_assoc_1() {
      TH1D *h_dphi = new TH1D("h_dphi", "#Delta#phi Distribution; #Delta#
     phi; Entries", 64, -TMath::Pi()/2, 3*TMath::Pi()/2);
      TH1D *h_trig = new TH1D("h_trig", "p_{T}^{trig}) Distributuion", 50
     , 0, 10);
      TFile *file = TFile::Open("/home/vishnu/Documents/Pheno/
     output_pPb_nonSat.root");
      TTree *tree = (TTree*)file->Get("Kinematic Variable");
      vector < double > *Eta_1a = new vector < double >;
      vector < double > *Phi_1b = new vector < double >;
      vector < double > *pT_1d = new vector < double >;
      vector<int> *multiplicity_1c = new vector<int>;
      vector < double > *particleId_1e = new vector < double >;
      tree->SetBranchAddress("Eta_1a", &Eta_1a);
      tree->SetBranchAddress("Phi_1b", &Phi_1b);
14
      tree->SetBranchAddress("pT_1d", &pT_1d);
      tree->SetBranchAddress("multiplicity_1c", &multiplicity_1c);
      tree->SetBranchAddress("particleId_1e", &particleId_1e);
17
18
      int nEntries = tree->GetEntries();
      cout << nEntries << endl;</pre>
      double trigger = 0;
      for(int i = 0; i < nEntries; ++i) {</pre>
          tree->GetEntry(i);
          if((*multiplicity_1c)[i] < 200) continue;// and (*</pre>
     multiplicity_1c)[i]<150) continue;</pre>
          for(int j = 0; j < pT_1d->size(); ++j) {
               if((*particleId_1e)[j] == 111){
                   if((*pT_1d)[j] > 2.0 and (*Eta_1a)[j] >2.5 and (*Eta_1a
     )[j] < 5) {
                   h_trig->Fill((*pT_1d)[j]);
```

```
trigger++;
29
                    for(int k = 0 ; k < pT_1d->size(); ++k) {
30
                        if((*pT_1d)[k] < 2 \text{ and } (*pT_1d)[k] > 0.5 \text{ and } k!=j
      and (*Eta_1a)[j] >2.5 and (*Eta_1a)[j] <5 ) {</pre>
                             double dphi = (*Phi_1b)[j] - (*Phi_1b)[k];
32
                             if( dphi < -TMath::Pi()/2) dphi = dphi + 2*TMath</pre>
      ::Pi();
                             else if(dphi > 3*TMath::Pi()/2) dphi = dphi - 2*
34
      TMath::Pi();
                             h_dphi->Fill(dphi);
36
                        }
                    }
                    }
39
               }
40
           }
41
      }
43
44
      h_dphi->Scale((1.0/trigger)); //*(0.580341/0.548474));
46
      TFile *file1 = TFile::Open("/home/vishnu/Documents/Pheno/pT_cut/
47
      dphi_pPb_nonSat_pT_2.root", "RECREATE"); // Replace with desired
      output file name
      file1->cd();
48
      h_dphi->Write();
49
      h_trig->Write();
      file1->Close();
51
<sub>52</sub> }
```

References

- [1] E. Iancu, A. Leonidov, and L. D. McLerran, Phys. Lett. B510, 133 (2001) https://doi.org/10.48550/arXiv.hep-ph/0102009
- [2] Y. L. Dokshitzer, Sov. Phys. JETP 46, 641-653 (1977) S. Roesler, R. Engel, and J. Ranft, p. 1033 (2000).
- Ε. C. J. Η. Lee |3| L.Zheng, Aschenauer, and Phys. В. W. Rev. D 074037 Xiao. **89**, no.7. (2014)https://doi.org/10.1103/PhysRevD.89.074037 [arXiv:1403.2413 |hep-ph||.
- [4] E. Braidot [STAR], Nucl. Phys. A **854**, 168-174 (2011) doi:10.1016/j.nuclphysa.2011.01.016 [arXiv:1008.3989 [nucl-ex]].
- [5] J. Adams et al. [STAR], Phys. Rev. Lett. 97, 152302 (2006)
 doi:10.1103/PhysRevLett.97.152302 [arXiv:nucl-ex/0602011 [nucl-ex]].
- [6] I. Arsene et al. [BRAHMS], Phys. Rev. Lett. 93, 242303 (2004) doi:10.1103/PhysRevLett.93.242303 [arXiv:nucl-ex/0403005 [nucl-ex]].
- [7] S. Acharya et al. [ALICE], JHEP $\mathbf{06}$, 024 (2023) doi:10.1007/JHEP06(2023)024 [arXiv:2204.11732 [nucl-ex]].
- [8] J. L. Albacete and C. Marquet, Phys. Lett. B 687, 174-179 (2010)
 doi:10.1016/j.physletb.2010.02.073 [arXiv:1001.1378 [hep-ph]].
- [9] E. Braidot, "Two-particle azimuthal correlations at forward rapidity in STAR," [arXiv:1102.0931 [nucl-ex]].

- [10] C. Marquet, Nucl. Phys. A **796**, 41-60 (2007) doi:10.1016/j.nuclphysa.2007.09.001 [arXiv:0708.0231 [hep-ph]].
- [11] Wolpert, Robert. "The JETSCAPE Framework." ArXiv: Nuclear Theory, 2019.
- [12] A. H. Rezaeian, M. Siddikov, M. Van de Klundert and R. Venugopalan, PoS **DIS2013**, 060 (2013) doi:10.22323/1.191.0060 [arXiv:1307.0165 [hep-ph]].
- [13] H. Kowalski and D. Teaney, Phys. Rev. D 68, 114005 (2003) doi:10.1103/PhysRevD.68.114005 [arXiv:hep-ph/0304189 [hep-ph]].
- [14] B. Schenke, S. Schlichting, P. Tribedy and R. Venugopalan, Nucl. Phys. A 982, 263-266 (2019) doi:10.1016/j.nuclphysa.2018.09.036 [arXiv:1807.05632 [nucl-th]].
- [15] B. Schenke, P. Tribedy and R. Venugopalan, Nucl. Phys. A 931, 288-292 (2014) doi:10.1016/j.nuclphysa.2014.08.039
- [16] B. Schenke, P. Tribedy and R. Venugopalan, Phys. Rev. Lett. 108, 252301 (2012) doi:10.1103/PhysRevLett.108.252301 [arXiv:1202.6646 [nucl-th]].
- [17] The ePIC Collaboration. Electron-ion collider, https://www.bnl.gov/eic.
- [18] R. Abdul Khalek.... Science requirements and detector concepts for the electron-ion collider: EIC yellow report. Nuclear Physics A, 1026:122447, 2022. ISSN 0375-9474. doi: https://doi.org/10.1016/j.nuclphysa.2022.122447.